J Nonlinear Sci (2018) 28:147–191
https://doi.org/10.1007/s00332-017-9405-2

Journal of Nonlinear Science

Orientational Order on Surfaces: The Coupling of Topology, Geometry, and Dynamics

M. Nestler[1] · **I. Nitschke**[1] · **S. Praetorius**[1] · **A. Voigt**[1]

Received: 27 July 2016 / Accepted: 3 July 2017 / Published online: 24 July 2017
© Springer Science+Business Media, LLC 2017

Abstract We consider the numerical investigation of surface bound orientational order using unit tangential vector fields by means of a gradient flow equation of a weak surface Frank–Oseen energy. The energy is composed of intrinsic and extrinsic contributions, as well as a penalization term to enforce the unity of the vector field. Four different numerical discretizations, namely a discrete exterior calculus approach, a method based on vector spherical harmonics, a surface finite element method, and an approach utilizing an implicit surface description, the diffuse interface method, are described and compared with each other for surfaces with Euler characteristic 2. We demonstrate the influence of geometric properties on realizations of the Poincaré–Hopf theorem and show examples where the energy is decreased by introducing additional orientational defects.

Communicated by Robert V. Kohn.

Electronic supplementary material The online version of this article (doi:10.1007/s00332-017-9405-2) contains supplementary material, which is available to authorized users.

✉ M. Nestler
michael.nestler@tu-dresden.de

I. Nitschke
ingo.nitschke@tu-dresden.de

S. Praetorius
simon.praetorius@tu-dresden.de

A. Voigt
axel.voigt@tu-dresden.de

[1] Institut für Wissenschaftliches Rechnen, Technische Universität Dresden, Zellescher Weg 12–14, 01062 Dresden, Germany

Keywords Polar liquid crystals · Curved surface · Nematic shell · Intrinsic–extrinsic free energy

Mathematics Subject Classification 58J35 · 53C21 · 53A05 · 53A45 · 58K45 · 30F15

List of symbols

Derivatives

div	Surface divergence
grad	Surface gradient
rot	Surface curl
$\Delta_{\mathcal{S}}$	Surface Laplace–Beltrami operator
$\boldsymbol{\Delta}^{\mathrm{dR}}$	Surface Laplace–deRham operator

Discrete Exterior Calculus

e	Edge, $e \in \mathcal{E}$
$\star e$	Dual edge of e (Voronoi edge)
$\mathcal{E}$	Set of edges, with number $\lvert\mathcal{E}\rvert$
$\mathbf{e}$	Edge vector along edge e
$\mathbf{e}_\star$	Dual edge vector along dual chain $\star e$
T	Face, $T \in \mathcal{T}$
$\mathcal{T}$	Set of faces, with number $\lvert\mathcal{T}\rvert$
$*$	Hodge star operator
$\flat$	Lowering indices
$\sharp$	Rising indices
$\boldsymbol{\alpha}$	1-Form, $\boldsymbol{\alpha} \in \Lambda^1(\mathcal{S})$
α_h	Discrete 1-form, $\alpha_h \in \Lambda_h^1(\mathcal{K})$
$\underline{\boldsymbol{\alpha}}$	Primal-dual 1-form, $\underline{\boldsymbol{\alpha}} = (\alpha_h, *\alpha_h)$
$\mathcal{K}$	Simplicial complex
v	Vertex, $v \in \mathcal{V}$
$\star v$	Dual vertex (voronoi cell)
$\mathcal{V}$	Set of vertices, with number $\lvert\mathcal{V}\rvert$
$\mathbf{d}$	Exterior derivative

Geometry

Γ_{ij}^k	Christoffel symbols of second kind
θ	Colatitude coordinate, $\theta \in [0, \pi]$
φ	Azimuthal coordinate, $\varphi \in [0, 2\pi)$
ξ	Coordinate in normal direction of the surface
κ	Gaussian curvature

$\mathcal{H}$	Mean curvature $\mathcal{H} = \operatorname{div} \boldsymbol{\nu}$
Ω	Domain, $\Omega \subset \mathbb{R}^3$
E_{IJK}	Levi–Civita symbols
$\mathbf{g}$	Riemannian metric tensor
$\lvert\mathbf{g}\rvert$	Determinant of $\mathbf{g}$
π	Coordinate projection $\pi : \Omega_\delta \to \mathcal{S}$
$\pi_{\mathsf{T}\mathcal{S}}$	Surface projection $\pi_{\mathsf{T}\mathcal{S}} : \mathsf{T}\mathbb{R}^3 \to \mathsf{T}\mathcal{S}$
$\mathcal{B}$	Shape operator $\mathcal{B} = -\operatorname{grad} \boldsymbol{\nu}$
$\mathcal{S}$	Surface, i.e., compact closed oriented Riemannian 2-dim. manifold
$\chi(\mathcal{S})$	Characteristic of the surface $\mathcal{S}$
$\mathcal{S}^E$	Ellipsoidal surface
$\boldsymbol{\nu}$	Outer surface normal
$\mathbb{S}^2$	Unit 2-sphere
$\mathsf{T}\mathcal{S}$	Tangent bundle of surface $\mathcal{S}$
$\mathsf{T}^*\mathcal{S}$	Cotangent bundle of surface $\mathcal{S}$

Modeling

K	Uniform Frank constant
ω_n	Penalty constant for normality
ω_t	Penalty constant for tangentiality
$F^{\mathcal{S}}_{\omega_\mathrm{n}}$	Weak surface Frank–Oseen energy
ϵ_f	Error in the defect fusion time
ϵ_e	(Normalized) Mean energy error
t_k	Discrete time step
τ_k	Time step width in the kth time step

Phase Field

ϕ	Phase-field variable
$\delta_{\mathcal{S}}$	Surface delta function
W	Double well, $W(\phi) \simeq \delta_{\mathcal{S}}$
ζ	Double-well regularization
ε	Interface thickness of phase field
$d_{\mathcal{S}}(\mathbf{x})$	Signed-distance function

1 Introduction

We consider surface bound systems of densely packed rodlike particles that tend to align tangentially. The systems are modeled by a mesoscopic field theoretical description using an average direction and an order parameter, measuring the local variance of alignment toward this average direction. In flat space, an uniformly ordered ground state can be established. This is no longer true for curved space, which induces distortions of this ground state, eventually inhibiting the propagation of preferred orientational order throughout the whole system. This leads to the emergence of defects,

which for surfaces $\mathcal{S}$ with Euler characteristic $\chi(\mathcal{S}) \neq 0$ is a consequence of the Poincaré–Hopf theorem. However, the type of the defects, their number, as well as their position are mostly unknown. The realization of the Poincaré–Hopf theorem depends on geometric properties of the surface and dynamics of the evolution. It is the goal of this paper to provide numerical methods to explore these interesting and non-trivial connections between topology, geometry, and dynamics. Besides the mathematical issues, the problem is of interest in the physics and materials science community due to its envisioned technological applications (Nelson 2002).

We focus on orientational ordering in polar order dynamics. The model follows as limit of a thin-film formulation of a modified Frank–Oseen energy (Frank 1958) and is formulated as an L^2-gradient flow, which leads to a vector-valued partial differential equation on the surface. Previous work has postulated a purely intrinsic formulation, extending the flat space model to curved space (Nelson 1983; Lubensky and Prost 1992; Lopez-Leon et al. 2011). More recent research (Napoli and Vergori 2012a, b; Segatti et al. 2014) derives a surface Frank–Oseen energy as limit of a thin-film formulation. This approach adds to the intrinsic model an explicit influence of the embedding space by extrinsic quantities. However, the limit is only established for surfaces with $\chi(\mathcal{S}) = 0$ and only allows defect free configurations. All approaches focus only on the steady state and utilize continuous optimization methods (Kralj et al. 2011) or Monte Carlo-based methods (Blumberg Selinger et al. 2011; Li et al. 2014; Nguyen et al. 2013) to evaluate the minimizers. To complement these models and methods, we derive a more general thin-film limit, valid also for surfaces with $\chi(\mathcal{S}) \neq 0$, and focus on the dynamics of orientational order on such surfaces.

Starting from the general surface modeling provided in Sect. 2, we establish suitable reformulations to apply different numerical methods and solve the resulting dynamic equations. We propose methods based on a coordinate-free framework as well as methods adapted for the Cartesian coordinates of the embedding $\mathbb{R}^3$ by using a penalty term approach. Section 3 gives the general notations, and Sect. 4 presents the methods of discrete exterior calculus (DEC), vector spherical harmonics (SPH), surface finite elements (sFEM), and diffuse interface modeling (DI). We compare results of these methods in Sect. 5 to provide estimations on numerical quality and computational cost. Further, we use these methods to perform experiments investigating the influence of geometry on emergence and energetical stability of non-minimal defect configurations and demonstrate the possibility to decrease the energy by introducing additional defects. The model formulations and proposed methods will provide a modeling and numerical toolkit ready to be applied to polar orientational order in curved space and related physical systems out of equilibrium. This and the implication for solving vector-valued partial differential equations on surfaces will be discussed in Sect. 6.

2 Model Derivation

Two major continuous theories to describe orientational order in liquid crystals exist. On the one hand, the Frank–Oseen theory uses a vector field to describe average molecular ordering, while, on the other hand, the Landau–de Gennes theory is based on a matrix expression (called Q-tensor). Both models are widely used and indeed coincide in flat 2D space for a specific set of elastic terms, see Ball and Zarnescu (2011), Iyer

et al. (2015). Besides this agreement, the Frank–Oseen modeling cannot account for a physical head-to-tail symmetry of the material, which is naturally considered in the Landau–de Gennes theory. For a mathematical review on both modeling approaches, we refer to Ball (2016). Due to its relative simplicity, we here consider only the Frank–Ossen theory as a modeling framework. Being aware of the fact that additional physical effects will occur within a corresponding Landau–de Gennes theory.

In our framework, the average alignment of anisometric molecules can be expressed by a unit vector $\mathbf{p}$, in the following called director, that represents the direction of the average alignment axis. In order to describe the spatial variation of a director field, a free energy F can be formulated that incorporates energy costs due to spatial distortions. The energy reads in simplified form (Oswald and Pieranski 2005)

$$F_{\mathrm{F}}\left[\mathbf{p}, \Omega\right] = \frac{1}{2}\int_{\Omega} K_1 \left(\nabla \cdot \mathbf{p}\right)^2 + K_2 \left(\mathbf{p} \cdot \left(\nabla \times \mathbf{p}\right)\right)^2 + K_3 \left\|\mathbf{p} \times \left(\nabla \times \mathbf{p}\right)\right\|^2 \mathrm{d}V, \quad (1)$$

with K_1, K_2, and K_3 the Frank phenomenological constants and $\Omega \subset \mathbb{R}^3$ a three-dimensional domain. The functional F_{F} contains three contributions related to deformations of $\mathbf{p}$, namely (from left to right) for splay, twist, and bend. We here consider the one-constant approximation $K := K_1 = K_2 = K_3$. The distortion energy thus reads

$$F_{\mathrm{OC}}\left[\mathbf{p}, \Omega\right] = \frac{K}{2}\int_{\Omega} \left(\nabla \cdot \mathbf{p}\right)^2 + \left\|\nabla \times \mathbf{p}\right\|^2 \mathrm{d}V. \quad (2)$$

To arrive at a surface formulation, we consider a thin shell $\Omega = \Omega_\delta$ around a compact smooth Riemannian surface $\mathcal{S}$, with thickness δ sufficiently small, and $\mathbf{p}$ parallel to the surface and parallel transported in normal direction to the surface. The limiting case of $F_{\mathrm{OC}}\left[\mathbf{p}, \Omega_\delta\right]$, $\delta \searrow 0$, where Ω_δ collapses to the surface, has been considered in Napoli and Vergori (2012b) for surfaces with $\chi(\mathcal{S}) = 0$ and thus only for defect free configurations. This result cannot simply be extended to more general surfaces, as a smooth vector field with unit norm exists if and only if $\chi(\mathcal{S}) = 0$. This topological result can also be extended to the corresponding Sobolev space (Segatti et al. 2016) and thus turns out to be useless for any investigation of defects in unit vector fields on surfaces. While in mathematical terms these defects can be considered as discontinuities, in physical terms the liquid crystal undergoes a phase transition to an isotropic phase at the defect. To enable a continuous director field $\mathbf{p}$ and to incorporate this phase transition, we drop the constraint $\|\mathbf{p}\| = 1$ and consider $\|\mathbf{p}\|$ as an order parameter. This parameter ranges from 0, describing the isotropic phase, to 1, for the ordered phase of the liquid crystal. To enforce a prevalent ordered phase, we add a well-known quartic state potential to the free energy with penalty parameter ω_{n}. It is evident that the radius of the defect core, the domain where the local alignment breaks down, is closely connected to ω_{n}. Since we are interested in orientational ordering of a prevalent ordered state, we choose $\omega_{\mathrm{n}} \gg K$, effectively enforcing defects with small core radius. The corresponding energy reads

$$F_{\omega_{\mathrm{n}}}\left[\mathbf{p}, \Omega\right] = \frac{K}{2}\int_{\Omega} \left(\nabla \cdot \mathbf{p}\right)^2 + \left\|\nabla \times \mathbf{p}\right\|^2 \mathrm{d}V + \frac{\omega_{\mathrm{n}}}{4}\int_{\Omega} \left(\left\|\mathbf{p}\right\|^2 - 1\right)^2 \mathrm{d}V. \quad (3)$$

Now, the limit $\delta \searrow 0$ can be considered also for $\chi(\mathcal{S}) \neq 0$, see "Appendix A." We obtain $\lim_{\delta \searrow 0} \frac{1}{\delta} F_{\omega_\mathrm{n}}\left[\mathbf{p}, \Omega_\delta\right] = F^{\mathcal{S}}_{\omega_\mathrm{n}}[\mathbf{p}]$, which we call the *weak surface Frank–Oseen energy*

$$F^{\mathcal{S}}_{\omega_\mathrm{n}}[\mathbf{p}] = F^{\mathcal{S}}_{\mathrm{I}}[\mathbf{p}] + F^{\mathcal{S}}_{\mathrm{E}}[\mathbf{p}] + \frac{\omega_\mathrm{n}}{4} \int_{\mathcal{S}} \left(\|\mathbf{p}\|^2 - 1 \right)^2 \, \mathrm{d}\mathcal{S}. \tag{4}$$

It consists of an intrinsic contribution $F^{\mathcal{S}}_{\mathrm{I}}[\mathbf{p}]$ and an extrinsic contribution $F^{\mathcal{S}}_{\mathrm{E}}[\mathbf{p}]$ to the distortion energy, as in Napoli and Vergori (2012a, b), and the additional penalty term, which contain the 2-norm $\|\cdot\|$. In the following, we assume $\mathbf{p} \in \mathsf{T}\mathcal{S}$ the tangent bundle of $\mathcal{S}$. Then, the intrinsic distortion energy $F^{\mathcal{S}}_{\mathrm{I}}$ can be expressed in terms of the surface divergence "div" and the surface curl "rot" of $\mathbf{p}$:

$$F^{\mathcal{S}}_{\mathrm{I}}[\mathbf{p}] = \frac{K}{2} \int_{\mathcal{S}} (\operatorname{div} \mathbf{p})^2 + (\operatorname{rot} \mathbf{p})^2 \, \mathrm{d}\mathcal{S}\,. \tag{5}$$

Introducing further the shape operator $\mathcal{B} = -\operatorname{grad} \boldsymbol{\nu}$ of $\mathcal{S}$ with outer surface normal $\boldsymbol{\nu}$, the extrinsic contributions can be written as

$$F^{\mathcal{S}}_{\mathrm{E}}[\mathbf{p}] = \frac{K}{2} \int_{\mathcal{S}} \|\mathcal{B} \cdot \mathbf{p}\|^2 \, \mathrm{d}\mathcal{S}. \tag{6}$$

Putting all parts together, we finally obtain

$$F^{\mathcal{S}}_{\omega_\mathrm{n}}[\mathbf{p}] = \frac{K}{2} \int_{\mathcal{S}} (\operatorname{div} \mathbf{p})^2 + (\operatorname{rot} \mathbf{p})^2 + \|\mathcal{B} \cdot \mathbf{p}\|^2 \, \mathrm{d}\mathcal{S} + \frac{\omega_\mathrm{n}}{4} \int_{\mathcal{S}} \left(\|\mathbf{p}\|^2 - 1 \right)^2 \mathrm{d}\mathcal{S}. \tag{7}$$

For the description of the minimization of $F^{\mathcal{S}}_{\omega_\mathrm{n}}[\mathbf{p}]$, we define the function spaces

$$H(\operatorname{div}, \mathcal{S}, \mathsf{T}\mathcal{S}) := \left\{ \mathbf{p} \in L^2(\mathcal{S};\, \mathsf{T}\mathcal{S}) \;:\; \operatorname{div} \mathbf{p} \in L^2(\mathcal{S}) \right\},$$
$$H(\operatorname{rot}, \mathcal{S}, \mathsf{T}\mathcal{S}) := \left\{ \mathbf{p} \in L^2(\mathcal{S};\, \mathsf{T}\mathcal{S}) \;:\; \operatorname{rot} \mathbf{p} \in L^2(\mathcal{S}) \right\},$$

and furthermore the space $H^{\mathrm{DR}}(\mathcal{S};\, \mathsf{T}\mathcal{S}) := H(\operatorname{div}, \mathcal{S}, \mathsf{T}\mathcal{S}) \cap H(\operatorname{rot}, \mathcal{S}, \mathsf{T}\mathcal{S})$. The minimization of the weak surface Frank–Oseen energy reads

$$\mathbf{p}^* = \operatorname{argmin} \left\{ F^{\mathcal{S}}_{\omega_\mathrm{n}}[\mathbf{p}] \;:\; \mathbf{p} \in H^{\mathrm{DR}}(\mathcal{S};\, \mathsf{T}\mathcal{S}) \right\}.$$

In Chen (1989), Segatti et al. (2014), the convergence of minimizers of $F^{\mathcal{S}}_{\omega_\mathrm{n}}$ to the sharp energy $F^{\mathcal{S}}_{\mathrm{I}}[\mathbf{p}] + F^{\mathcal{S}}_{\mathrm{E}}[\mathbf{p}]$, as $\omega_\mathrm{n} \to \infty$, is analyzed and proven for the case $\chi(\mathcal{S}) = 0$.

Dynamical equations to minimize the functional $F^{\mathcal{S}}_{\omega_\mathrm{n}}$ can be formulated by means of an L^2-gradient flow approach,

$$\partial_t \mathbf{p} = -\frac{\delta F^{\mathcal{S}}_{\omega_\mathrm{n}}}{\delta \mathbf{p}}[\mathbf{p}],$$

where the gradient of $F^{\mathcal{S}}_{\omega_\mathrm{n}}$ has to be interpreted w.r.t. the $L^2(\mathcal{S};\,\mathsf{T}\mathcal{S})$ inner product. For $\mathbf{q} \in H^{\mathrm{DR}}(\mathcal{S};\,\mathsf{T}\mathcal{S})$, this reads

$$\begin{aligned}
&\int_{\mathcal{S}} \left\langle \frac{\delta F^{\mathcal{S}}_{\omega_\mathrm{n}}}{\delta \mathbf{p}}[\mathbf{p}],\, \mathbf{q} \right\rangle \mathrm{d}\mathcal{S} \\
&\quad = \int_{\mathcal{S}} -K\,(\operatorname{div}\mathbf{p}\operatorname{div}\mathbf{q} + \operatorname{rot}\mathbf{p}\operatorname{rot}\mathbf{q}) + K\langle \mathcal{B}\mathbf{p},\, \mathcal{B}\mathbf{q}\rangle + \omega_\mathrm{n}\big(\,\|\mathbf{p}\|^2 - 1\big)\langle \mathbf{p},\, \mathbf{q}\rangle\,\mathrm{d}\mathcal{S} \\
&\quad = \int_{\mathcal{S}} K\langle \boldsymbol{\Delta}^{\mathrm{dR}}\mathbf{p},\, \mathbf{q}\rangle + K\langle \mathcal{B}^2\mathbf{p},\, \mathbf{q}\rangle + \omega_\mathrm{n}\big(\,\|\mathbf{p}\|^2 - 1\big)\langle \mathbf{p},\, \mathbf{q}\rangle\,\mathrm{d}\mathcal{S},
\end{aligned}$$

with $\boldsymbol{\Delta}^{\mathrm{dR}}$ the Laplace–deRham operator. This leads to the evolution equation

$$\partial_t \mathbf{p} + K\left(\boldsymbol{\Delta}^{\mathrm{dR}}\mathbf{p} + \mathcal{B}^2\mathbf{p}\right) + \omega_\mathrm{n}\left(\|\mathbf{p}\|^2 - 1\right)\mathbf{p} = 0, \quad \text{in } \mathcal{S}\times(0,\infty) \tag{8}$$

with the initial condition $\mathbf{p}\,(t=0) = \mathbf{p}^0 \in \mathsf{T}\mathcal{S}$. The gradient flow approach guarantees dissipative dynamics and stationary solutions of (8) as local minima of $F^{\mathcal{S}}_{\omega_\mathrm{n}}$. Note that the sign of the vectorial Laplacian is different from the sign of the scalar Laplacian found in classical diffusion-like equations, since we follow the convention of Abraham et al. (1988).

Introducing the covariant director $\boldsymbol{\alpha} := \mathbf{p}^\flat \in \mathsf{T}^*\mathcal{S}$, an equivalent formulation of Eq. (8) in terms of its dual vectors can be stated:

$$\partial_t \boldsymbol{\alpha} + K\left(\boldsymbol{\Delta}^{\mathrm{dR}}\boldsymbol{\alpha} + \mathcal{B}^2\boldsymbol{\alpha}\right) + \omega_\mathrm{n}\left(\|\boldsymbol{\alpha}\|^2 - 1\right)\boldsymbol{\alpha} = 0, \tag{9}$$

with $\boldsymbol{\alpha}^0 = (\mathbf{p}^0)^\flat \in \mathsf{T}^*\mathcal{S}$, where we have used the notation of a musical isomorphism $\flat$ to denote the flattening operation. Both formulations of the gradient flow problem, (8) and (9), are implemented in the present paper by means of several numerical approaches.

3 Notation

We consider a compact closed oriented Riemannian two-dimensional manifold $\mathcal{S} \subset \mathbb{R}^3$ parametrized by the local coordinates θ, φ:

$$\mathbf{x} : \mathbb{R}^2 \supset U \to \mathbb{R}^3;\ (\theta,\varphi) \mapsto \mathbf{x}\,(\theta,\varphi)\ . \tag{10}$$

Thus, the embedded $\mathbb{R}^3$ representation of the surface is given by $\mathcal{S} = \mathbf{x}(U)$. The unit outer normal of $\mathcal{S}$ at point $\mathbf{x}$ is denoted by $\boldsymbol{\nu}(\mathbf{x})$. An implicit description of the surface is given by the signed-distance function

$$d_{\mathcal{S}}(\widetilde{\mathbf{x}}) := \begin{cases} -\inf_{\mathbf{y}\in\mathcal{S}} \|\widetilde{\mathbf{x}} - \mathbf{y}\| & \text{for } \widetilde{\mathbf{x}} \in G \\ \inf_{\mathbf{y}\in\mathcal{S}} \|\widetilde{\mathbf{x}} - \mathbf{y}\| & \text{for } \widetilde{\mathbf{x}} \in \mathbb{R}^3 \setminus \bar{G} \end{cases}, \tag{11}$$

with a bounded open set $G \subset \mathbb{R}^3$ and $\partial G = \mathcal{S}$. The corresponding extended surface normal $\widetilde{\boldsymbol{\nu}} : \mathbb{R}^3 \to \mathbb{R}^3$ can be calculated by

$$\widetilde{\boldsymbol{\nu}} := \frac{\nabla d_{\mathcal{S}}}{\|\nabla d_{\mathcal{S}}\|}, \quad \text{with } \widetilde{\boldsymbol{\nu}}\big|_{\mathcal{S}} = \boldsymbol{\nu} \text{ and } \|\nabla d_{\mathcal{S}}\| = 1, \tag{12}$$

see, e.g., Dziuk and Elliott (2013).

The key ingredient in differential geometry and tensor analysis on Riemannian manifolds is the positive definite metric tensor

$$\mathbf{g} = \begin{bmatrix} g_{\theta\theta} & g_{\theta\varphi} \\ g_{\theta\varphi} & g_{\varphi\varphi} \end{bmatrix} = g_{\theta\theta}\, d\theta^2 + 2g_{\theta\varphi}\, d\theta\, d\varphi + g_{\varphi\varphi}\, d\varphi^2. \tag{13}$$

The covariant components of the metric tensor are given by $\mathbb{R}^3$ inner products of partial derivatives of $\mathbf{x}$, i.e., $g_{ij} = \partial_i \mathbf{x} \cdot \partial_j \mathbf{x}$. The components of the inverse tensor $\mathbf{g}^{-1}$ are denoted by g^{ij} and the determinant of $\mathbf{g}$ by $|\mathbf{g}|$. We denote by $\{\partial_\theta \mathbf{x}, \partial_\varphi \mathbf{x}\}$ the canonical basis to describe contravariant (tangential) vectors $\mathbf{p}(\mathbf{x}) \in \mathsf{T}_{\mathbf{x}}\mathcal{S}$, i.e., $\mathbf{p} = p^\theta \partial_\theta \mathbf{x} + p^\varphi \partial_\varphi \mathbf{x}$ at a point $\mathbf{x} \in \mathcal{S}$. Furthermore, with the arising dual basis $\{d\theta, d\varphi\}$ we are able to write an arbitrary 1-form (covariant vector) $\boldsymbol{\alpha} \in \mathsf{T}^*_{\mathbf{x}}\mathcal{S}$ as $\boldsymbol{\alpha} = p_\theta d\theta + p_\varphi d\varphi$. This identifier choice of the covariant vector coordinates p_i in conjunction with representation of $\mathbf{p}$ as above implies that $\boldsymbol{\alpha}$ and $\mathbf{p}$ are related by $\boldsymbol{\alpha} = \mathbf{p}^\flat$ and $\mathbf{p} = \boldsymbol{\alpha}^\sharp$, respectively. Explicitly lowering and rising the indices can be done using the metric tensor $\mathbf{g}$ by $p_i = g_{ij} p^j$ and $p^i = g^{ij} p_j$, respectively.

In a (tubular) neighborhood Ω_δ of $\mathcal{S}$, defined by $\Omega_\delta := \{\widetilde{\mathbf{x}} \in \mathbb{R}^3 : d_{\mathcal{S}}(\widetilde{\mathbf{x}}) < \frac{1}{2}\delta\}$, a coordinate projection $\mathbf{x} \in \mathcal{S}$ of $\widetilde{\mathbf{x}} \in \mathbb{R}^3$ is introduced, such that

$$\widetilde{\mathbf{x}} = \mathbf{x} + d_{\mathcal{S}}(\widetilde{\mathbf{x}})\boldsymbol{\nu}(\mathbf{x}). \tag{14}$$

For δ sufficiently small (depending on the local curvature of the surface), this projection is injective, see Dziuk and Elliott (2013). For a given $\widetilde{\mathbf{x}} \in \Omega_\delta$, the coordinate projection of $\widetilde{\mathbf{x}}$ will also be called gluing map, denoted by $\pi : \Omega_\delta \to \mathcal{S}$, $\widetilde{\mathbf{x}} \mapsto \mathbf{x}$.

Scalar functions $f : \mathcal{S} \to \mathbb{R}$ and vector fields $\mathbf{p} : \mathcal{S} \to \mathsf{T}\mathcal{S}$ can be smoothly extended in the neighborhood Ω_δ of $\mathcal{S}$ by utilizing the coordinate projection, i.e., extended fields $\tilde{f} : \Omega_\delta \to \mathbb{R}$ and $\tilde{\mathbf{p}} : \Omega_\delta \to \mathbb{R}^3$ are defined by

$$\tilde{f}(\widetilde{\mathbf{x}}) := f(\mathbf{x}) \quad \text{and} \quad \tilde{\mathbf{p}}(\widetilde{\mathbf{x}}) := \mathbf{p}(\mathbf{x}), \tag{15}$$

respectively, for $\widetilde{\mathbf{x}} \in \Omega_\delta$ and $\mathbf{x}$ the corresponding coordinate projection. This extension can be realized by implementing a Hopf–Lax formula on discrete grids representing the surface and its neighborhood, similar to a redistancing method, see Bornemann and Rasch (2006), Burger et al. (2008).

Table 1 Various representations of the inner product and first-order differential operators on surfaces for scalar fields $f : \mathcal{S} \to \mathbb{R}$ and tangential vector fields $\mathbf{p}, \mathbf{q} : \mathcal{S} \to \mathsf{T}\mathcal{S}$ or $\mathbb{R}^3$ vector fields $\widehat{\mathbf{p}} : \mathcal{S} \to \mathsf{T}\mathbb{R}^3 \cong \mathbb{R}^3$ are listed

Symbolic	Local coord.	$\mathbb{R}^3$ coord.	EC
$\langle \mathbf{p}, \mathbf{q} \rangle$	$p_i q^i$	$\widehat{\mathbf{p}} \cdot \mathbf{q}$	$*(\boldsymbol{\alpha} \wedge *\boldsymbol{\beta})$
grad f	$g^{ij} \partial_j f \partial_i \mathbf{x}$	$\pi_{\mathsf{T}\mathcal{S}} \nabla f$	$\mathbf{d} f$
rot f	$\frac{1}{\sqrt{\lvert\mathbf{g}\rvert}} \left(\partial_\theta f \partial_\varphi \mathbf{x} - \partial_\varphi f \partial_\theta \mathbf{x} \right)$	$\boldsymbol{\nu} \times \nabla f$	$*\mathbf{d} f$
div $\mathbf{p}$	$\partial_i p^i + \frac{1}{\sqrt{\lvert\mathbf{g}\rvert}} p^i \partial_i \sqrt{\lvert\mathbf{g}\rvert}$	$\nabla \cdot \widehat{\mathbf{p}} - \boldsymbol{\nu} \cdot (\nabla \widehat{\mathbf{p}} \cdot \boldsymbol{\nu})$	$*\mathbf{d} * \boldsymbol{\alpha}$
rot $\mathbf{p}$	$\frac{1}{\sqrt{\lvert\mathbf{g}\rvert}} \left(\partial_\theta p_\varphi - \partial_\varphi p_\theta \right)$	$(\nabla \times \widehat{\mathbf{p}}) \cdot \boldsymbol{\nu}$	$*\mathbf{d}\boldsymbol{\alpha}$

Vector-valued images are represented in a contravariant form. In the formulation in $\mathbb{R}^3$ coordinates, the scalar field f and vector field $\widehat{\mathbf{p}}$ with respect to the Euclidean basis $\{\mathbf{e}^x, \mathbf{e}^y, \mathbf{e}^z\}$ are assumed to be defined in a neighborhood of $\mathcal{S}$. In the column "Exterior Calculus" (EC), all is in the space of 1-forms that are related to the vector fields $\mathbf{p}$ by $\boldsymbol{\alpha} = \mathbf{p}^\flat$, $\boldsymbol{\beta} = \mathbf{q}^\flat$ and the images can be compared with other columns by rising the indices

3.1 Function Spaces

For scalar fields $f, g : \mathcal{S} \to \mathbb{K} \in \{\mathbb{R}, \mathbb{C}\}$ and vector fields $\mathbf{p}, \mathbf{q} : \mathcal{S} \to \mathsf{T}\mathcal{S}$, an L^2 inner product is given by

$$(f,\ g)_{L^2(\mathcal{S})} := \int_{\mathcal{S}} f\, \bar{g}\, \mathrm{d}\mathcal{S}, \tag{16}$$

$$(\mathbf{p},\ \mathbf{q})_{L^2(\mathcal{S};\, \mathsf{T}\mathcal{S})} := \int_{\mathcal{S}} \langle \mathbf{p},\ \bar{\mathbf{q}} \rangle\ \mathrm{d}\mathcal{S}, \tag{17}$$

respectively, with $\bar{g}$, $\bar{\mathbf{q}}$ the complex conjugates[1] and $\langle \cdot,\ \cdot \rangle$ the local inner product, see Table 1. These L^2 inner products define the corresponding $L^2(\mathcal{S})$ and $L^2(\mathcal{S};\, \mathsf{T}\mathcal{S})$ Hilbert spaces, respectively.

3.2 Differential Calculus

There are many ways to describe classical differential operators on surfaces. The choice of representation arises from the context that we want to use. In Table 1 first-order differential operations on scalars and vector fields and an inner product are summarized and listed for the specific context.

With introduced local coordinate chart above, we can use the inner metric $\mathbf{g}$ and partial derivatives ∂ (column "Local coord." in Table 1). In the Euclidean space $\mathbb{R}^3$, where the surface is embedded, it is possible to describe the differential operators using $\mathbb{R}^3$ operators like $\cdot$, $\times$ or ∇ and the surface normal $\boldsymbol{\nu}$. The extension from the surface $\mathcal{S}$ to $\mathbb{R}^3$ rises some choices of embedding the $\mathbb{R}^3$ vector space structure to

[1] In the spherical harmonics method, the functions are complex-valued, and thus, we need a complex L^2 inner product. For all real-valued functions, the complex conjugation can be ignored.

the tangential bundle of the surface. We use in this paper a pointwise defined normal projection

$$\begin{aligned} &\pi_{\mathsf{T}\mathcal{S}}(\mathbf{x}) : \mathsf{T}_{\mathbf{x}}\mathbb{R}^3 \cong \mathbb{R}^3 \to \mathsf{T}_{\mathbf{x}}\mathcal{S}; \\ &\widehat{\mathbf{p}}(\mathbf{x}) \mapsto \widehat{\mathbf{p}}(\mathbf{x}) - \boldsymbol{\nu}(\mathbf{x})(\boldsymbol{\nu}(\mathbf{x}) \cdot \widehat{\mathbf{p}}(\mathbf{x})) = \mathbf{p}(\mathbf{x}) \end{aligned} \tag{18}$$

for all $\mathbf{x} \in \mathcal{S}$, which maps an $\mathbb{R}^3$ vector $\widehat{\mathbf{p}} = p_x\,\mathbf{e}^x + p_y\,\mathbf{e}^y + p_z\,\mathbf{e}^z \in \mathbb{R}^3$, not necessarily tangential to the surface, to a tangential vector $\mathbf{p} \in \mathsf{T}_{\mathbf{x}}\mathcal{S}$. We drop the argument $\mathbf{x}$ when applied to vector fields living on $\mathcal{S}$. Some flexibility arises in the choice of the first-order differential operators for non-tangential vector fields defined on $\mathcal{S}$, see the operators listed in column "$\mathbb{R}^3$ coord." in Table 1. With this notation, we can express the shape operator as a linear map $\mathcal{B} = \{\mathcal{B}^i_{\ j}\} : \mathsf{T}\mathcal{S} \to \mathsf{T}\mathcal{S}$ in local and $\mathbb{R}^3$ coordinates by

$$\mathcal{B}^i_{\ j} = -g^{ik}\left(\partial_j \boldsymbol{\nu} \cdot \partial_k \mathbf{x}\right) \quad i,j,k = 1,2 \quad \text{and} \quad \mathcal{B}_{ij} = -\left[\operatorname{grad} \nu_j\right]_i \quad i,j = 1,2,3, \tag{19}$$

respectively. This operator is symmetric, i.e., $\langle \mathbf{q}, \mathcal{B}\mathbf{p}\rangle = \langle \mathbf{p}, \mathcal{B}\mathbf{q}\rangle$ for all $\mathbf{p}, \mathbf{q} \in \mathsf{T}\mathcal{S}$. For the shape operator on the dual space in local coordinates

$${}^{\flat}\mathcal{B}^{\sharp} = \left\{ g_{ik}\mathcal{B}^k_{\ l} g^{lj} \right\} = \left\{ \mathcal{B}_i^{\ j} \right\} : \mathsf{T}^*\mathcal{S} \to \mathsf{T}^*\mathcal{S}, \tag{20}$$

we will omit the superscripts $\sharp$ and $\flat$ and write $\mathcal{B}$ shortly, if it is clear on which object the shape operator is acting. Throughout these definitions, we require the operators to coincide with surface operators for tangential fields.

From a physical point of view, neither $\mathbf{p} \in \mathsf{T}\mathcal{S}$ nor the differential operator listed in column "Symbolic" in Table 1 need explicitly defined coordinate charts. Such a coordinate-free formulation ensures conformance in every smooth coordinate system. In the context of exterior calculus (EC), a graded associative algebra referring to the wedge product $\wedge$ and differential forms is introduced to implement such a coordinate-free formulation. All fundamental first-order differential operators listed in column "EC" in Table 1 can be described by the Hodge star $*$ and the exterior derivative $\mathbf{d}$, which arise algebraically, see Abraham et al. (1988) for details.

The Laplace operators in this paper can be obtained by composing first-order operators. The Rot-Rot-Laplace and Grad-Div-Laplace for vector-valued functions (and 1-forms) are defined by

$$\boldsymbol{\Delta}^{\mathrm{RR}}\mathbf{p} := \operatorname{rot}\operatorname{rot}\mathbf{p} \qquad \text{and} \qquad \boldsymbol{\Delta}^{\mathrm{GD}}\mathbf{p} := \operatorname{grad}\operatorname{div}\mathbf{p}. \tag{21}$$

In Abraham et al. (1988), the Laplace–deRham operator is defined for k-forms on an n-dimensional Riemannian manifold by $\boldsymbol{\Delta}^{\mathrm{dR}} := (-1)^{nk+1}\,(*\mathbf{d}*\mathbf{d} + \mathbf{d}*\mathbf{d}*)$.

For vector fields, we define the Laplace–deRham operator canonically as composition ($\sharp \circ \boldsymbol{\Delta}^{\mathrm{dR}} \circ \flat$). Finally, we obtain

$$\boldsymbol{\Delta}^{\mathrm{dR}}\mathbf{p} = -\left(\boldsymbol{\Delta}^{\mathrm{RR}} + \boldsymbol{\Delta}^{\mathrm{GD}}\right)\mathbf{p}. \tag{22}$$

for vector-valued functions (and 1-forms) $\mathbf{p}$ (and $\boldsymbol{\alpha}$).

4 Numerical Methods

The growing interest in partial differential equations on surfaces is driven by various applications, but also by challenging numerical problems, which result from the nonlinearity due to the underlying curved space. Various numerical methods have been developed to deal with these problems for scalar-valued surface partial differential equations. Finite element spaces are constructed on triangulated surface (Dziuk 1988; Dziuk and Elliott 2007a, b). These surface finite elements essentially allow to use the same concepts and tools as in flat space (Vey and Voigt 2007; Dziuk and Elliott 2013), and also the computational cost is comparable. The same holds for finite volume methods on quadrilateral grids on surfaces (Calhoum et al. 2008). Other approaches consider an implicit representation of the surface, either through a level set description (Bertalmio et al. 2001; Greer et al. 2006; Stöcker and Voigt 2008; Dziuk and Elliott 2008), within a diffuse interface approximation (Rätz and Voigt 2006, 2007) or a closest point method (Ruuth and Merriman 2008; Macdonald and Ruuth 2008). All these methods only require minimal information on the surface. All geometric information is constructed solely through knowledge of the vertices of the discretization, or through the implicit description of a level set, phase-field function, or point cloud. This has been proven to be sufficient and leads to efficient numerical methods also for complex physical problems (Eilks and Elliott 2008; Lowengrub et al. 2009; Aland et al. 2011; Rätz and Röger 2012; Aland et al. 2012; Nitschke et al. 2012; Stoop et al. 2015).

For vector-valued surface partial differential equations, the coupling between the equation and the geometry is much stronger and numerical methods which reduce the geometric information to a minimum might no longer be the most efficient. The literature on numerical methods for such problems is rare and mainly restricted to special surfaces, like the sphere. Here, spectral methods based on spherical harmonics expansions are a popular tool (Backus 1966; Barrera et al. 1985; Freeden et al. 1994; Kostelec et al. 2000; Fengler and Freeden 2005; Freeden and Schreiner 2009). Another method which makes use of detailed geometric properties is an exterior calculus approach (Hirani 2003; Desbrun et al. 2005; Arnold et al. 2006, 2010), which has recently also been applied to vector-valued surface partial differential equations, e.g., surface Navier–Stokes equations (Mohamed et al. 2016; Nitschke et al. 2016).

We will consider four different methods to solve the weak surface Frank–Oseen problem (8) and (9). The first method is a discrete exterior calculus (DEC) formulation of Eq. (9), to be discussed in Sect. 4.2. To handle the penalty term requires an implementation of a pair of discrete equations for the dual vector and its hodge-dual variant and leads to a coupled system of primal-dual equations, which to the best of our knowledge has not been considered before in this context. In Sect. 4.3, the second method based on spherical harmonics (SPH) is introduced. This approach expands $\mathbf{p}$ in a spherical function basis, given as eigenfunctions of the Laplace–deRham

operator. This results in a discrete set of equation for the expansion coefficients. The third approach is the surface finite element method (sFEM), to be explained in Sect. 4.4. It relaxes the requirement of $\mathbf{p}$ to be a tangential field, by introducing an additional penalty term that weakly enforces tangentiality. The vector field is represented in an Euclidean basis, leading to a system of scalar-valued surface PDEs. The representation of the Laplace–deRham operator in an Euclidean basis incooperating the penalty terms is a new ansatz to discretize vector-valued surface PDEs. The fourth method is the diffuse interface method (DI), see Sect. 4.5. It extends the domain to the embedding space $\mathbb{R}^3$, enforces tangentiality weakly, and additionally restricts the differential operators to the surface using an approximation of a surface delta function. This leads to a system of coupled scalar-valued PDEs in a three-dimensional domain and extends the established concept to vector-valued surface PDEs.

In the following section, the time discretization for the evolution problem is introduced. It is shared by all considered methods.

4.1 Discretization in Time

Let $0 < t_0 < t_1 < \cdots$ be a sequence of time steps with time step width $\tau_k := t_{k+1} - t_k$ in the kth iteration. The fields $\mathbf{p}^k(\mathbf{x}) \equiv \mathbf{p}(\mathbf{x}, t_k)$ and $\boldsymbol{\alpha}^k(\mathbf{x}) \equiv \boldsymbol{\alpha}(\mathbf{x}, t_k)$, respectively, correspond to the time-discrete functions at t_k. Applying a semi-implicit Euler discretization to (8) and (9) results in time-discrete systems of equations as follows: let $\mathbf{p}^0 \in C(\mathcal{S};\, \mathsf{T}\mathcal{S})$ be a given initial director field. For $k = 0, 1, 2, \ldots$ find $\mathbf{p}^{k+1} \in C^2(\mathcal{S};\, \mathsf{T}\mathcal{S})$ s.t.

$$\frac{1}{\tau_k}\mathbf{p}^{k+1} + K\left(\boldsymbol{\Delta}^{\mathrm{dR}}\mathbf{p}^{k+1} + \mathcal{B}^2\mathbf{p}^{k+1}\right) + \omega_{\mathrm{n}} f\left(\mathbf{p}^k, \mathbf{p}^{k+1}\right) = \frac{1}{\tau_k}\mathbf{p}^k \quad \text{in } \mathcal{S}, \tag{23}$$

with $f(\mathbf{p}^k, \mathbf{p}^{k+1}) \approx (\|\mathbf{p}^{k+1}\|^2 - 1)\mathbf{p}^{k+1}$ a linearization of the nonlinear term. In the methods DEC, sFEM, and DI we consider a linear Taylor expansion around $\mathbf{p}^k$, see (24), and in the method SPH we implement an explicit evaluation at the old time step t_k, see (25):

$$f^{\mathrm{Taylor}}\left(\mathbf{p}^k, \mathbf{p}^{k+1}\right) := \left(\|\mathbf{p}^k\|^2 - 1\right)\mathbf{p}^{k+1} + 2\left\langle \mathbf{p}^{k+1}, \mathbf{p}^k \right\rangle \mathbf{p}^k - 2\|\mathbf{p}^k\|^2\mathbf{p}^k \tag{24}$$

$$f^{\mathrm{expl}}\left(\mathbf{p}^k, \mathbf{p}^{k+1}\right) := \|\mathbf{p}^k\|^2\mathbf{p}^k - \mathbf{p}^{k+1}. \tag{25}$$

The corresponding time discretization of the dual vector formulation (9) is similar to (23) utilizing the correspondence between vectors and dual vectors by the musical isomorphism $\flat$ for the initial condition: Let $\boldsymbol{\alpha}_0 := \mathbf{p}_0^\flat$ be given. For $k = 0, 1, 2, \ldots$ find $\boldsymbol{\alpha}_{k+1} \in \Lambda^1(\mathcal{S})$ s.t.

$$\frac{1}{\tau_k}\boldsymbol{\alpha}^{k+1} + K\left(\boldsymbol{\Delta}^{\mathrm{dR}}\boldsymbol{\alpha}^{k+1} + \mathcal{B}^2\boldsymbol{\alpha}^{k+1}\right) + \omega_{\mathrm{n}} f\left(\boldsymbol{\alpha}^k, \boldsymbol{\alpha}^{k+1}\right) = \frac{1}{\tau_k}\boldsymbol{\alpha}^k \quad \text{in } \mathcal{S}. \tag{26}$$

4.2 DEC

For a discrete exterior calculus, the surface discretization is a simplicial complex $\mathcal{K} = \mathcal{V} \sqcup \mathcal{E} \sqcup \mathcal{T}$ containing sets of vertices $\mathcal{V}$, edges $\mathcal{E}$, and (triangular) faces $\mathcal{T}$. The quantities of interest in our DEC discretization are 1-forms $\boldsymbol{\alpha} \in \Lambda^1(\mathcal{S}) = \mathsf{T}^*\mathcal{S}$. We do not approximate the coordinate function of $\boldsymbol{\alpha}$ on a discrete set of points or vertices, but rather introduce a finite set of degrees of freedom (DOFs) as integral values on the edges $e \in \mathcal{E}$,

$$\alpha_h(e) := \int_{\pi(e)} \boldsymbol{\alpha}, \tag{27}$$

with the gluing map $\pi : \mathcal{E} \to \mathcal{S}$, which projects geometrically the edge e to the surface $\mathcal{S}$. The mapping $\alpha_h \in \Lambda_h^1(\mathcal{K})$ is called the discrete 1-form of $\boldsymbol{\alpha}$, since $\alpha_h(e)$ approximates $\boldsymbol{\alpha}(e) \equiv \boldsymbol{\alpha}(\mathbf{e}) = \langle \mathbf{p}, \mathbf{e} \rangle$ on an intermediate point $\xi \in \pi(e) \subset \mathcal{S}$, where the edge vector $\mathbf{e}$ exists in $\mathsf{T}_\xi \mathcal{S}|_{\pi(e)}$ by the mean value theorem. Therefore, we approximate 1-forms on the restricted dual tangential space $\mathsf{T}_\xi \mathcal{S}|_{\pi(e)}$, which is a one-dimensional vector space in $\xi \in \mathcal{S}$ likewise the space of discrete 1-forms $\Lambda_h^1(\mathcal{K})|_e = \Lambda_h^1(\{e\})$ restricted to the edge e. Hence, a discrete 1-form problem on surfaces leads to a one-dimensional problem, like a scalar-valued problem.

The simplicial complex $\mathcal{K}$ is manifold-like, orientable and well centered. For a detailed discussion of these requirements and general introduction to DEC, see Hirani (2003), Desbrun et al. (2005).

Discrete linear differential operators composed of the exterior derivative $\mathbf{d}$ and the Hodge operator $*$, like the Laplace–deRham operator $\boldsymbol{\Delta}^{\mathrm{dR}}$, see Sect. 3, can be implemented by successively utilizing a discrete version of the Hodge operator and the Stokes theorem for the exterior derivative, see Hirani (2003). This procedure leads to a DEC discretized Rot-Rot-Laplace $\boldsymbol{\Delta}_h^{\mathrm{RR}}$ and Grad-Div-Laplace $\boldsymbol{\Delta}_h^{\mathrm{GD}}$. For discrete 1-forms $\alpha_h \in \Lambda_h^1(\mathcal{K})$, sign mappings $s_{\circ,\circ} \in \{-1, +1\}$, volumes $|\cdot|$, Voronoi cells $\star v$, Voronoi edges $\star e$, and the "belongs-to" relations $\succ$ and $\prec$, we obtain

$$\boldsymbol{\Delta}_h^{\mathrm{RR}} \alpha_h(e) = -\frac{|e|}{|\star e|} \sum_{T \succ e} \frac{s_{T,e}}{|T|} \sum_{\tilde{e} \prec T} s_{T,\tilde{e}}\, \alpha_h(\tilde{e}), \tag{28}$$

$$\boldsymbol{\Delta}_h^{\mathrm{GD}} \alpha_h(e) = -\sum_{v \prec e} \frac{s_{v,e}}{|\star v|} \sum_{\tilde{e} \succ v} s_{v,\tilde{e}} \frac{|\star \tilde{e}|}{|\tilde{e}|} \alpha_h(\tilde{e}). \tag{29}$$

Hence, in analogy to Sect. 3, we get the DEC discretized Laplace–deRham operator $\boldsymbol{\Delta}_h^{\mathrm{dR}} \alpha_h(e) = -(\boldsymbol{\Delta}_h^{\mathrm{RR}} \alpha_h(e) + \boldsymbol{\Delta}_h^{\mathrm{GD}} \alpha_h(e))$. See "Appendix D" for details in notation and derivation of the DEC operators. The value for $\boldsymbol{\Delta}_h^{\mathrm{dR}} \alpha_h(e)$ on an edge e is determined as a linear combination of few edge values $\alpha_h(\tilde{e})$ in a *proximate neighborhood* of e, i.e., it exists a vertex v that connects the edges $e \succ v$ and $\tilde{e} \succ v$.

Restricting the time-discrete evolution Eq. (26) to the edges, using (27), leads to a system of equations for all edges $e \in \mathcal{E}$:

$$\frac{1}{\tau_k} \alpha_h^{k+1}(e) + K \left(\boldsymbol{\Delta}_h^{\mathrm{dR}} \alpha_h^{k+1}(e) + \left(\mathcal{B}^2 \boldsymbol{\alpha}^{k+1} \right)_h (e) \right) + \omega_{\mathrm{n}} \left(f(\boldsymbol{\alpha}^k, \boldsymbol{\alpha}^{k+1}) \right)_h (e) = \frac{1}{\tau_k} \alpha_h^k(e), \tag{30}$$

with $(\mathcal{B}^2\boldsymbol{\alpha}^{k+1})_h(e) = \int_{\pi(e)} \mathcal{B}^2\boldsymbol{\alpha}^{k+1}$. Using Taylor expansion (24) in its covariant form, we obtain in the $(k+1)$th time step for the nonlinear term

$$\begin{aligned}\left(f\left(\boldsymbol{\alpha}^k, \boldsymbol{\alpha}^{k+1}\right)\right)_h(e) &= \int_{\pi(e)} \left(\|\boldsymbol{\alpha}^k\|^2 - 1\right)\boldsymbol{\alpha}^{k+1} + 2\left\langle\boldsymbol{\alpha}^{k+1}, \boldsymbol{\alpha}^k\right\rangle\boldsymbol{\alpha}^k - 2\|\boldsymbol{\alpha}^k\|^2\boldsymbol{\alpha}^k \\ &= \int_{\pi(e)} \left(\left(\|\boldsymbol{\alpha}^k\|^2 - 1\right)\mathrm{Id}_{\mathsf{T}^*\mathcal{S}} + 2\boldsymbol{\alpha}^k \otimes \left(\boldsymbol{\alpha}^k\right)^\sharp\right)\boldsymbol{\alpha}^{k+1} \\ &\quad - \int_{\pi(e)} 2\|\boldsymbol{\alpha}^k\|^2 \mathrm{Id}_{\mathsf{T}^*\mathcal{S}}\boldsymbol{\alpha}^k \\ &=: \left(\mathcal{L}^k\boldsymbol{\alpha}^{k+1}\right)_h(e) - \left(\mathcal{R}^k\boldsymbol{\alpha}^k\right)_h(e),\end{aligned} \tag{31}$$

with the identity map $\mathrm{Id}_{\mathsf{T}^*\mathcal{S}} : \mathsf{T}^*\mathcal{S} \to \mathsf{T}^*\mathcal{S}$.

In the remaining section, we discuss how to implement the norm $\|\alpha_h(e)\|$, the upcoming inner product $\langle\alpha_h(e), \alpha_h'(e)\rangle$ in the evaluation of the nonlinear term, and the endomorphisms $\mathcal{B}^2$, $\mathcal{L}^k$, and $\mathcal{R}^k$.

For the edge $e_0 := e$, we choose another edge e_1 in the proximate neighborhood of e_0. These two edges define a vector space $V_T := \mathrm{Span}\{\mathbf{e}_0, \mathbf{e}_1\}$ for the face $T \succ e_0, e_1$ at the contact vertex $v \prec e_0, e_1$. A barycentric parametrization of V_T, regarding the basis vectors, results in a flat discrete metric

$$\mathbf{g} = (\mathbf{e}_i \cdot \mathbf{e}_j) de^i de^j, \tag{32}$$

with the ordinary $\mathbb{R}^3$ dot product and the canonical dual basis $\left\{de^0, de^1\right\}$, which spans the flat vector space for covariant vectors. So, we can construct a 1-form $\underline{\boldsymbol{\alpha}}(e) \in \mathsf{T}^*V_T$, which is constant on T, by $\underline{\boldsymbol{\alpha}}(e) = \alpha_h(e_i)de^i$. Hence, if g^{ij} are the components of the inverse of the metric (32), the square of the norm is given by

$$\|\alpha_h(e)\|^2 \equiv \left\|\underline{\boldsymbol{\alpha}}(e)\right\|^2 = \alpha_h(e_i)g^{ij}\alpha_h(e_j). \tag{33}$$

This norm strongly depends on the choice of the additional edge e_1. Considering the Voronoi edge $\star e$ (see "Appendix D"), which is not an edge in a pure simplicial sense, but a chain containing two edges orthogonal to e, one on the left face $T_2 \succ e$ and one on the right face $T_1 \succ e$, i.e., $\star e = \star e|_{T_1} + \star e|_{T_2}$, leads to a stable pair of edges. With a piecewise linear barycentric parametrization $\boldsymbol{\gamma} : [0, 1] \to \star e$ of the polygonal chain $\star e$, with piecewise constant derivative $\|\boldsymbol{\gamma}'\| = |\star e|$ we can define the Voronoi edge vector

$$\mathbf{e}_\star := \boldsymbol{\gamma}' \in \mathsf{T}T_1 \sqcup \mathsf{T}T_2.$$

This leads to the discrete metric in terms of the orthogonal basis $\{\mathbf{e}, \mathbf{e}_\star\}$ and the dual basis $\{de, de^\star\}$,

$$\mathbf{g} = |e|^2 (de)^2 + |\star e|^2 \left(de^\star\right)^2 \tag{34}$$

and, with $\alpha_h(\star e) \approx -\frac{|\star e|}{|e|}(*\alpha_h)(e)$ (see Hirani 2003), the discrete (covariant) vector-valued 1-form

$$\underline{\boldsymbol{\alpha}}(e) = \alpha_h(e)de + \alpha_h(\star e)de^\star \approx \alpha_h(e)de - \frac{|\star e|}{|e|}(*\alpha_h)(e)de^\star. \tag{35}$$

The resulting vector spaces on all edges $e \in \mathcal{E}$ can be summarized as disjoint unions to $\mathfrak{T}\mathcal{E} := \bigsqcup_{e\in\mathcal{E}} \bigsqcup_{T\succ e} \mathrm{Span}\{\mathbf{e}, \mathbf{e}_\star|_T\}$. We call $\left(\alpha_h, *\alpha_h\right) := \underline{\boldsymbol{\alpha}} : \mathcal{E} \to \mathfrak{T}^*\mathcal{E}$ a *discrete primal-dual-1-form (PD-1-form)* with components α_h and $*\alpha_h$ in $\Lambda_h^1(\mathcal{K})$. Let $\Lambda_h^1(\mathcal{K}; \mathfrak{T}^*\mathcal{E})$ be the *space of discrete PD-1-forms*. All discrete PD-1-forms are uniquely defined and depend only on the edge e and geometrical information about it and its Voronoi edge. Henceforward, we omit the argument e for a better readability. The norm of $\underline{\boldsymbol{\alpha}} = \underline{\boldsymbol{\alpha}}(e)$ is computed on all edges e with the discrete metric (34) by

$$\left\|\underline{\boldsymbol{\alpha}}\right\|^2 = \frac{1}{|e|^2}\left(\alpha_h^2 + (*\alpha_h)^2\right) \tag{36}$$

and the discrete inner product with another discrete PD-1-form $\underline{\boldsymbol{\beta}} = \left(\beta_h, *\beta_h\right)$ is computed by

$$\left\langle \underline{\boldsymbol{\alpha}}, \underline{\boldsymbol{\beta}} \right\rangle = \frac{1}{|e|^2}\left(\alpha_h\beta_h + (*\alpha_h)(*\beta_h)\right). \tag{37}$$

The Hodge star operator applied to (26) results in the Hodge-dual equation

$$\frac{1}{\tau_k}(*\boldsymbol{\alpha})^{k+1} + K\left(\boldsymbol{\Delta}^{\mathrm{dR}}(*\boldsymbol{\alpha})^{k+1} + *\mathcal{B}^2\boldsymbol{\alpha}^{k+1}\right) + \omega_{\mathrm{n}} * f\left(\boldsymbol{\alpha}^k, \boldsymbol{\alpha}^{k+1}\right) = \frac{1}{\tau_k}(*\boldsymbol{\alpha})^k, \tag{38}$$

where the identity $*\boldsymbol{\Delta}^{\mathrm{dR}} = \boldsymbol{\Delta}^{\mathrm{dR}}*$ for the Laplace–deRham operator is used. Restricting (38) to the edges $e \in \mathcal{E}$, utilizing (27), and combining the result with (30) leads to

$$\begin{aligned}\frac{1}{\tau_k}\underline{\boldsymbol{\alpha}}^{k+1} + K\left(\boldsymbol{\Delta}^{\mathrm{dR}}\underline{\boldsymbol{\alpha}}^{k+1} + \begin{bmatrix}\left(\mathcal{B}^2\boldsymbol{\alpha}^{k+1}\right)_h \\ \left(*\mathcal{B}^2\boldsymbol{\alpha}^{k+1}\right)_h\end{bmatrix}\right) + \omega_{\mathrm{n}}\begin{bmatrix}\left(\mathcal{L}^k\boldsymbol{\alpha}^{k+1}\right)_h \\ \left(*\mathcal{L}^k\boldsymbol{\alpha}^{k+1}\right)_h\end{bmatrix} \\ = \frac{1}{\tau_k}\underline{\boldsymbol{\alpha}}^k + \omega_{\mathrm{n}}\begin{bmatrix}\left(\mathcal{R}^k\boldsymbol{\alpha}^k\right)_h \\ \left(*\mathcal{R}^k\boldsymbol{\alpha}^k\right)_h\end{bmatrix} \quad \text{in } \mathcal{E}.\end{aligned} \tag{39}$$

In "Appendix D," it is shown, how to approximate endomorphisms $\mathbf{M} : \mathsf{T}^*\mathcal{S} \to \mathsf{T}^*\mathcal{S}$ in a DEC-PD context, so that

$$\begin{bmatrix}(\mathbf{M}\boldsymbol{\alpha})_h \\ (*\mathbf{M}\boldsymbol{\alpha})_h\end{bmatrix} \approx \underline{\underline{\mathbf{M}}} \cdot \underline{\boldsymbol{\alpha}} \quad \text{in } \mathcal{E} \tag{40}$$

with the mixed co- and contravariant *discrete PD-(1,1)-Tensor* $\underline{\underline{\mathbf{M}}}$. Evaluating the $\mathbb{R}^3$ representation of the shape operator at the midpoint of the edge $e \in \mathcal{E}$ projected to the

surface, i.e., $\mathcal{B}^2(e) := \mathcal{B}^2|_{\pi(c(e))} \in \mathbb{R}^{3\times 3}$, utilizing (110), results in a matrix form of the shape operator, applicable in (40),

$$\underline{\underline{\mathcal{B}}}^2(e) = \begin{bmatrix} \frac{\mathbf{e}\cdot\mathcal{B}^2(e)\cdot\mathbf{e}}{|e|^2} & -\frac{\mathbf{e}\cdot\mathcal{B}^2(e)\cdot\mathbf{e}_\star}{|e||\star e|} \\ -\frac{\mathbf{e}_\star\cdot\mathcal{B}^2(e)\cdot\mathbf{e}}{|e||\star e|} & \frac{\mathbf{e}_\star\cdot\mathcal{B}^2(e)\cdot\mathbf{e}_\star}{|\star e|^2} \end{bmatrix}. \tag{41}$$

Similarly, with (36) and $\mathrm{Id}^\flat_{\mathsf{T}^*\mathcal{S}} = \mathbf{g}$, considering the discrete metric, we get

$$\underline{\underline{\mathcal{R}}}^k(e) = 2\left\|\underline{\boldsymbol{\alpha}}^k(e)\right\|^2 \begin{bmatrix} 1 & 0 \\ 0 & 1 \end{bmatrix}, \tag{42}$$

$$\begin{aligned} \underline{\underline{\mathcal{L}}}^k(e) &= \left(\left\|\underline{\boldsymbol{\alpha}}^k(e)\right\|^2 - 1\right)\begin{bmatrix} 1 & 0 \\ 0 & 1 \end{bmatrix} + 2\begin{bmatrix} \frac{\alpha_h^k(e)\alpha_h^k(e)}{|e|^2} & -\frac{\alpha_h^k(e)\alpha_h^k(\star e)}{|e||\star e|} \\ -\frac{\alpha_h^k(e)*\alpha_h^k(\star e)}{|e||\star e|} & \frac{\alpha_h^k(\star e)\alpha_h^k(\star e)}{|\star e|^2} \end{bmatrix} \\ &\approx \left(\left\|\underline{\boldsymbol{\alpha}}^k(e)\right\|^2 - 1\right)\begin{bmatrix} 1 & 0 \\ 0 & 1 \end{bmatrix} + \frac{2}{|e|^2}\begin{bmatrix} \alpha_h^k(e)\alpha_h^k(e) & \alpha_h^k(e)\,(*\alpha)_h^k(e) \\ \alpha_h^k(e)\,(*\alpha)_h^k(e) & (*\alpha)_h^k(e)\,(*\alpha)_h^k(e) \end{bmatrix} \\ &=: \underline{\underline{\tilde{\mathcal{L}}}}^k(e). \end{aligned} \tag{43}$$

Finally, with the discrete inner product (37), $\underline{\underline{\mathcal{R}}}^k \cdot \underline{\boldsymbol{\alpha}}^k = 2\left\|\underline{\boldsymbol{\alpha}}^k\right\|^2 \underline{\boldsymbol{\alpha}}^k$, and

$$\underline{\underline{\tilde{\mathcal{L}}}}^k \cdot \underline{\boldsymbol{\alpha}}^{k+1} = \left(\left\|\underline{\boldsymbol{\alpha}}^k\right\|^2 - 1\right)\underline{\boldsymbol{\alpha}}^{k+1} + 2\left\langle\underline{\boldsymbol{\alpha}}^{k+1}, \underline{\boldsymbol{\alpha}}^k\right\rangle\underline{\boldsymbol{\alpha}}^k \quad \text{in } \mathcal{E}, \tag{44}$$

the introduced Taylor linearization of f, i.e., $f^{\mathrm{Taylor}}(\underline{\boldsymbol{\alpha}}^k, \underline{\boldsymbol{\alpha}}^{k+1})$, is found.

This results in a series of time-discrete linear DEC-PD problems: For $k = 0, 1, 2, \ldots$, and a given initial value $\underline{\boldsymbol{\alpha}}^0$, find $\underline{\boldsymbol{\alpha}}^{k+1} \in \Lambda_h^1(\mathcal{K}; \mathfrak{T}^*\mathcal{E})$ s.t.

$$\frac{1}{\tau_k}\underline{\boldsymbol{\alpha}}^{k+1} + K\left(\boldsymbol{\Delta}^{\mathrm{dR}}\underline{\boldsymbol{\alpha}}^{k+1} + \underline{\underline{\mathcal{B}}}^2 \cdot \underline{\boldsymbol{\alpha}}^{k+1}\right) + \omega_{\mathrm{n}} f^{\mathrm{Taylor}}\left(\underline{\boldsymbol{\alpha}}^k, \underline{\boldsymbol{\alpha}}^{k+1}\right) = \frac{1}{\tau_k}\underline{\boldsymbol{\alpha}}^k \quad \text{in } \mathcal{E}. \tag{45}$$

These stationary problems can be implemented by assembling a matrix and vector for the components $\alpha_h(e)$ and $(*\alpha_h)(e)$ on edges $e \in \mathcal{E}$. The resulting linear system is solved with the TFQMR method, see Freund (1993).

There are many conceivable ways to interpolate the initial condition $\underline{\boldsymbol{\alpha}}^0 = [\alpha^0, *\alpha^0] \in \Lambda_h^1(\mathcal{K}; \mathfrak{T}^*\mathcal{E})$ from a given vector field $\mathbf{p}^0 \in T\mathcal{S}$. We assume that the simplicial complex and its polytope $|\mathcal{K}|$ are immersed in a sufficiently small neighborhood Ω_δ of the surface, so that the initial condition $\mathbf{p}^0$ can be smoothly extended.

Given such an extension $\widetilde{\mathbf{p}}^0$ of an initial vector field $\mathbf{p}^0$, we can choose the intersection point $c(e)$ of an edge $e \in \mathcal{E}$ and $\star e$ for approximating the integral expressions, i.e., let the edge e be given so that it points from the vertex v_1 to the vertex v_2 and the

dual edge $\star e$ from the circumcenter $c(T_1)$ to $c(T_2)$, then we obtain

$$\alpha^0(e) = \int_{\pi(e)} \left(\mathbf{p}^0\right)^\flat \approx \int_0^1 \widetilde{\mathbf{p}}^0\left(c(e)\right) \cdot \mathbf{e}\, \mathrm{d}\lambda = \widetilde{\mathbf{p}}^0\left(c(e)\right) \cdot (v_2 - v_1) \tag{46}$$

$$\begin{aligned}(*\alpha)^0(e) &\approx -\frac{|e|}{|\star e|} \int_{\star\pi(e)} \left(\mathbf{p}^0\right)^\flat \approx -\frac{|e|}{|\star e|} \int_0^1 \widetilde{\mathbf{p}}^0\left(c(e)\right) \cdot \mathbf{e}_\star\, \mathrm{d}\lambda \\ &= -\frac{|e|}{|\star e|} \widetilde{\mathbf{p}}^0(c(e)) \cdot \left(c\left(T_2\right) - c\left(T_1\right)\right). \end{aligned} \tag{47}$$

On the other hand, if $\mathbf{p}^0$ arise from the gradient of a scalar function $f : \mathcal{S} \to \mathbb{R}$, i.e., $\mathbf{p}^0 = \operatorname{grad} f = (\mathbf{d} f)^\sharp$, we obtain for a smooth extension $\widetilde{f}$ of f:

$$\alpha^0(e) = \int_{\pi(e)} \mathbf{d} f = f(v_2) - f(v_1) \tag{48}$$

$$\begin{aligned}(*\alpha)^0(e) &\approx -\frac{|e|}{|\star e|} \int_{\star\pi(e)} \mathbf{d} f \\ &\approx -\frac{|e|}{|\star e|} \left(\widetilde{f}(c(T_2)) - \widetilde{f}(c(T_1))\right), \end{aligned} \tag{49}$$

utilizing Stoke's theorem.

4.3 Spectral Method

In this section, we restrict our consideration to spherical surfaces $\mathcal{S} = \mathbb{S}^2$ parametrized by $\theta \in [0, \pi]$ and $\varphi \in [0, 2\pi)$, i.e., the colatitude and azimuthal coordinates, respectively. So each point $\mathbf{x}_{\mathbb{S}^2} \in \mathbb{S}^2$ can be written as $\mathbf{x}_{\mathbb{S}^2}(\theta, \varphi) = \sin(\theta)\cos(\varphi)\,\mathbf{e}^x + \sin(\theta)\sin(\varphi)\,\mathbf{e}^y + \cos(\theta)\,\mathbf{e}^z$. Based on the observation that the tangential part of a spherical vector field can be split into a curl-free and a divergence-free field by using derivatives of scalar fields, an efficient numerical methods can be constructed. The Helmholtz decomposition theorem (Freeden and Schreiner 2009) states that every continuously differentiable spherical tangent vector field $\mathbf{f} : \mathcal{S} \to \mathsf{T}\mathcal{S}$ can be represented by uniquely determined scalar functions $f_1, f_2 \in C^1(\mathcal{S})$ as

$$\mathbf{f}(\mathbf{x}) = \operatorname{grad} f_1(\mathbf{x}) + \operatorname{rot} f_2(\mathbf{x}).$$

An efficient solution method for linear surface PDEs on the sphere is based on a spectral expansion of the objective scalar functions $f \in L^2(\mathcal{S})$ in the spherical harmonics $Y_l^m : \mathcal{S} \to \mathbb{C}$, $(l, m) \in \mathcal{I}_\infty$ with $\mathcal{I}_N := \{(l, m) : 0 \le l \le N, -l \le m \le l\}$, which build an $L^2(\mathcal{S})$-orthonormal system of eigenfunctions of the Laplace–Beltrami operator $\Delta_\mathcal{S}$, i.e.,

$$\Delta_\mathcal{S} Y_l^m = \Delta_{lm} Y_l^m \quad \text{with } \Delta_{lm} := -l(l+1), \quad \text{for } (l, m) \in \mathcal{I}_\infty \tag{50}$$

and $\left(Y_l^m,\ Y_{l'}^{m'}\right)_{L^2(\mathcal{S})} = \delta_{ll'}\delta_{mm'}$, cf. Hesthaven et al. (2007), Backofen et al. (2011). Due to the symmetries of the sphere, analytic representations of Y_l^m can be found in terms of associated Legendre polynomials. This allows for an efficient evaluation of the basis functions.

A scalar function $f \in L^2(\mathcal{S})$ can be represented in the series expansion

$$f(\theta,\varphi) = \sum_{l=0}^{\infty}\sum_{m=-l}^{l} f_{lm} Y_l^m(\theta,\varphi) \tag{51}$$

with expansion coefficient $f_{lm} = \left(f,\ Y_l^m\right)_{L^2(\mathcal{S})}$.

Taking the gradient and curl of the spherical harmonics, an expansion for tangential vector fields can be constructed. Therefore, we introduce two vector spherical harmonics $\boldsymbol{y}_{lm}^{(1)},\ \boldsymbol{y}_{lm}^{(2)}$ as

$$\begin{aligned} \boldsymbol{y}_{lm}^{(1)}(\theta,\varphi) &:= N_{lm}\ \mathrm{grad}\ Y_l^m(\theta,\varphi), \\ \boldsymbol{y}_{lm}^{(2)}(\theta,\varphi) &:= N_{lm}\ \mathrm{rot}\ Y_l^m(\theta,\varphi) \end{aligned} \tag{52}$$

with normalization constants $N_{lm} = (-\Delta_{lm}^{-1})^{1/2}$. These functions are normalized in such a way that they build again an $L^2(\mathcal{S};\ \mathsf{T}\mathcal{S})$-orthonormal system of eigenfunctions of a Laplace operator, namely the spherical Laplace–deRham operator (Freeden et al. 1994; Freeden and Schreiner 2009), i.e.,

$$\boldsymbol{\Delta}^{\mathrm{dR}} \boldsymbol{y}_{lm}^{(i)} = -\Delta_{lm} \boldsymbol{y}_{lm}^{(i)}, \quad \text{for } i = 1,2,\ (l,m) \in \mathcal{I}_\infty \tag{53}$$

and $\left(\boldsymbol{y}_{lm}^{(i)},\ \boldsymbol{y}_{l'm'}^{(j)}\right)_{L^2(\mathcal{S};\,\mathsf{T}\mathcal{S})} = \delta_{ij}\delta_{ll'}\delta_{mm'}$.

A series expansion of a tangent vector field $\mathbf{f} \in L^2(\mathcal{S};\ \mathsf{T}\mathcal{S})$, based on the expansion of scalar fields (51) and the gradient and curl basis representation (52), can thus be written as

$$\mathbf{f}(\theta,\varphi) = \sum_{i=1}^{2}\sum_{l=0}^{\infty}\sum_{m=-l}^{l} f_{lm}^{(i)} \boldsymbol{y}_{lm}^{(i)}(\theta,\varphi) \tag{54}$$

with expansion coefficients $f_{lm}^{(i)} = \left(\mathbf{f},\ \boldsymbol{y}_{lm}^{(i)}\right)_{L^2(\mathcal{S};\,\mathsf{T}\mathcal{S})}$. In the following, we use the notation $\underline{\mathbf{f}}_{lm} := \left(f_{lm}^{(1)},\ f_{lm}^{(2)}\right)$ to denote the pair of coefficients.

The spherical harmonics method is based on the idea to approximate any scalar function (51) and vector-valued function (54) by truncated expansions with bandwidth $l_{\max} =: N$. Therefore, we introduce the space of spherical vector polynomials

$$\vec{\Pi}_N(\mathcal{S}) := \left\{ \mathbf{f} = \sum_{i=1}^{2}\sum_{l=0}^{N}\sum_{m=-l}^{l} f_{lm}^{(i)} \boldsymbol{y}_{lm}^{(i)} \right\}.$$

The evaluation of expansion coefficients, in other words, the calculation of the L^2 inner product, is implemented by approximating the integral by an appropriate quadrature

rule. Let $\mathcal{V} = \{\mathbf{x}_k = (\theta_k, \varphi_k)\}$ be a set of quadrature points on the sphere and $\{w_k\}$ the corresponding quadrature weights. We introduce the discrete L^2 inner product:

$$\left(\mathbf{f},\ \boldsymbol{y}_{lm}^{(i)}\right)_{h,L^2(\mathcal{S};\mathsf{T}\mathcal{S})} := \sum_k w_k \left\langle \mathbf{f}(\theta_k, \varphi_k),\ \bar{\mathbf{y}}_{lm}^{(i)}(\theta_k, \varphi_k)\right\rangle.$$

In order to derive an equation for the expansion coefficients $\underline{\mathbf{p}}_{lm}$ of $\mathbf{p} \in \vec{\Pi}_N(\mathcal{S})$ in terms of a Galerkin approach, see, e.g., Hesthaven et al. (2007), we require the residual $\boldsymbol{r}$ of the differential Eq. (8),

$$\boldsymbol{r} := \frac{1}{\tau_k}\left(\mathbf{p}^{k+1} - \mathbf{p}^k\right) + K\left(\boldsymbol{\Delta}^{\mathrm{dR}}\mathbf{p}^{k+1} + \mathcal{B}^2\mathbf{p}^{k+1}\right) + \omega_{\mathrm{n}} f\left(\mathbf{p}^k, \mathbf{p}^{k+1}\right),$$

to be orthogonal to the basis of $\vec{\Pi}_N(\mathcal{S})$ w.r.t. the L^2 inner product, i.e.,

$$\left(\boldsymbol{r},\ \boldsymbol{y}_{lm}^{(i)}\right)_{L^2(\mathcal{S};\mathsf{T}\mathcal{S})} = 0, \quad \text{for } i = 1, 2,\ (l, m) \in \mathcal{I}_N. \tag{55}$$

The shape operator on the unit sphere simplifies to the surface identity, i.e., $\mathcal{B} = -\pi_{\mathsf{T}\mathcal{S}}$. With $f := f^{\mathrm{expl}}$, this term can be evaluated in discrete grid points on the sphere rather than by forming convolution sums of the coefficients, see Boyd (2001). Therefore, let the nonlinear term $\mathbf{f}^k := \|\mathbf{p}^k\|^2\mathbf{p}^k$ at time step t_k be expanded in the space $\vec{\Pi}_N(\mathcal{S})$ with expansion coefficients $\underline{\mathbf{f}}_{lm}^k$.

By requiring the new time step solution $\mathbf{p}^{k+1}$ to be an element of $\vec{\Pi}_N(\mathcal{S})$, we can insert the truncated expansion of the solution into the residual Eq. (55). Utilizing the property that the Laplace–deRham operator is the eigenoperator of the basis functions results in an equation for the expansion coefficients directly. Finally, the time step procedure for the spherical harmonics approach reads: Let

$$\underline{\mathbf{p}}_{lm}^{0,(i)} = \left(\mathbf{p}^0,\ \boldsymbol{y}_{lm}^{(i)}\right)_{h,L^2(\mathcal{S};\mathsf{T}\mathcal{S})} \qquad \text{for } i = 1, 2,\ (l, m) \in \mathcal{I}_N$$

be the expansion coefficients for the initial solution. For $k = 0, 1, 2, \ldots$

1. Evaluate $\mathbf{f}^k(\mathbf{x}) := \|\mathbf{p}^k(\mathbf{x})\|^2\mathbf{p}^k(\mathbf{x})$ for all $\mathbf{x} \in \mathcal{V}$.
2. Calculate $f_{lm}^{k,(i)} = \left(\mathbf{f}^k,\ \boldsymbol{y}_{lm}^{(i)}\right)_{h,L^2(\mathcal{S};\mathsf{T}\mathcal{S})}$ for $i = 1, 2,\ (l, m) \in \mathcal{I}_N$.
3. Solve

$$\frac{1}{\tau_k}\underline{\mathbf{p}}_{lm}^{k+1} - K\,\Delta_{lm}\underline{\mathbf{p}}_{lm}^{k+1} + (K - \omega_{\mathrm{n}})\underline{\mathbf{p}}_{lm}^{k+1} = \frac{1}{\tau_k}\underline{\mathbf{p}}_{lm}^{k} - \omega_{\mathrm{n}}\underline{\mathbf{f}}_{lm}^{k}, \quad \forall (l, m) \in \mathcal{I}_N$$

   to be understood componentwise.
4. Evaluate (54) with coefficients $\underline{\mathbf{p}}_{lm}^{k+1}$ to get $\mathbf{p}^{k+1}$.

The discrete spherical harmonics transform, that is, the evaluation of (51) for a bandwidth N, can be split up into a discrete Fourier transform, realizable by a fast Fourier transform, and discrete Legendre transforms, realizable by discrete cosine

transforms (Kunis and Potts 2003) or a fast multipole method (Suda and Takami 2002). The inverse transform, i.e., the calculation of the expansion coefficients, may be realized by the Gauss–Legendre algorithm. There, the integral is replaced by a Gauss–Legendre quadrature rule with Gauss nodes and weights in latitudinal direction (Schaeffer 2013). Therefore, the spherical coordinate space is discretized by the set of vertices

$$\mathcal{V} := \left\{ \mathbf{x}(\theta_i, \varphi_j) \,:\, 0 \le i < N_\theta,\, 0 \le j < N_\varphi \right\},$$

with θ_i Gauss nodes in $[0, \pi]$ and φ_j equally distributed in $[0, 2\pi)$. To respect the sampling theorem, we have chosen $N_\theta > N$ and $N_\varphi > 2N$. Therewith, the coefficients of the nonlinear term are only approximated, since $\mathbf{f}^k$ is not in $\vec{\Pi}_N(\mathcal{S})$ for $\mathbf{p}^k \in \vec{\Pi}_N(\mathcal{S})$.

Finally, the discrete vector harmonics transform can be implemented by two scalar transforms, see, e.g., Kostelec et al. (2000). Thus, the complexity of the transform is dominated by the scalar transform that can be realized in $\mathcal{O}(N^2 \log N)$ (Suda and Takami 2002).

4.4 Surface Finite Elements

We consider a reformulation of $F^{\mathcal{S}}_{\omega_\mathrm{n}}$ and dynamic Eq. (8) suitable for a componentwise surface finite element approximation. To do so, we extend $F^{\mathcal{S}}_{\omega_\mathrm{n}}$ to a domain of vector-valued functions $\widehat{\mathbf{p}} : \mathcal{S} \to \mathsf{T}\mathbb{R}^3$ and penalize any energy contributions by normal components $\widehat{\mathbf{p}} \cdot \boldsymbol{\nu} \neq 0$ with a penalty factor $\omega_\mathrm{t} \gg 1$. The previously introduced Laplace–deRham operator has been defined as a differential operator on sections of tangent bundles. This needs to be extended to $\mathbb{R}^3$ vector fields. In a first step, we use the surface projection $\pi_{\mathsf{T}\mathcal{S}}$ introduced in (18) and a result from (Duduchava et al. 2006) to express $\operatorname{div} \mathbf{p}$ by $\operatorname{div} \widehat{\mathbf{p}}$, i.e.,

$$\operatorname{div} \mathbf{p} = \operatorname{div} \left(\pi_{\mathsf{T}\mathcal{S}} \widehat{\mathbf{p}} \right) = \underbrace{\nabla \cdot \widehat{\mathbf{p}} - \boldsymbol{\nu} \cdot \left(\nabla \widehat{\mathbf{p}} \cdot \boldsymbol{\nu} \right)}_{= \operatorname{div} \widehat{\mathbf{p}}} - \mathcal{H} \left(\widehat{\mathbf{p}} \cdot \boldsymbol{\nu} \right), \tag{56}$$

where $\mathcal{H} = \operatorname{div} \boldsymbol{\nu}$ denotes the mean curvature of $\mathcal{S}$. Note that the curl of a vector field reduces to the curl of its tangential part, i.e., $\operatorname{rot} \mathbf{p} = \operatorname{rot} \widehat{\mathbf{p}}$. Further, we apply a decomposition of $\widehat{\mathbf{p}} = \mathbf{p} + \boldsymbol{\nu} \left(\widehat{\mathbf{p}} \cdot \boldsymbol{\nu} \right)$ and $\widehat{\mathbf{q}} = \mathbf{q} + \boldsymbol{\nu} \left(\widehat{\mathbf{q}} \cdot \boldsymbol{\nu} \right)$ to express the L^2 inner product of $\boldsymbol{\Delta}^{\mathrm{dR}} \mathbf{p}$ and $\mathbf{q}$ in terms of $\widehat{\mathbf{p}}$ and $\widehat{\mathbf{q}}$ (for details, see "Appendix B"),

$$\begin{aligned} \int_{\mathcal{S}} \langle \boldsymbol{\Delta}^{\mathrm{dR}} \mathbf{p}, \mathbf{q} \rangle \, \mathrm{d}\mathcal{S} = & \int_{\mathcal{S}} \left(\operatorname{div} \widehat{\mathbf{p}} \right) \left(\operatorname{div} \widehat{\mathbf{q}} \right) + \left(\operatorname{rot} \widehat{\mathbf{p}} \right) \left(\operatorname{rot} \widehat{\mathbf{q}} \right) \mathrm{d}\mathcal{S} + \int_{\mathcal{S}} \mathcal{H}^2 \left(\widehat{\mathbf{p}} \cdot \boldsymbol{\nu} \right) \left(\widehat{\mathbf{q}} \cdot \boldsymbol{\nu} \right) \mathrm{d}\mathcal{S} \\ & - \int_{\mathcal{S}} \mathcal{H} \left(\left(\widehat{\mathbf{q}} \cdot \boldsymbol{\nu} \right) \left(\operatorname{div} \widehat{\mathbf{p}} \right) + \left(\widehat{\mathbf{p}} \cdot \boldsymbol{\nu} \right) \left(\operatorname{div} \widehat{\mathbf{q}} \right) \right) \mathrm{d}\mathcal{S}. \end{aligned}$$

In order to neglect the terms involving normal components $\left(\widehat{\mathbf{p}} \cdot \boldsymbol{\nu} \right)$ and $\left(\widehat{\mathbf{q}} \cdot \boldsymbol{\nu} \right)$, the penalty term $\frac{\omega_\mathrm{t}}{2} \left(\widehat{\mathbf{p}} \cdot \boldsymbol{\nu} \right)^2$ is added to the energy $F^{\mathcal{S}}_{\omega_\mathrm{n}}$. The functional derivative of this contribution results in a symmetric term

$$\int_{\mathcal{S}} \frac{\omega_\mathrm{t}}{2} \left\langle \frac{\delta(\widehat{\mathbf{p}} \cdot \boldsymbol{\nu})^2}{\delta \widehat{\mathbf{p}}}[\widehat{\mathbf{p}}], \widehat{\mathbf{q}} \right\rangle \mathrm{d}\mathcal{S} = \int_{\mathcal{S}} \omega_\mathrm{t} \, (\widehat{\mathbf{p}} \cdot \boldsymbol{\nu}) \, (\widehat{\mathbf{q}} \cdot \boldsymbol{\nu}) \, \mathrm{d}\mathcal{S} \tag{57}$$

leading in the context of a minimization process to $(\widehat{\mathbf{p}} \cdot \boldsymbol{\nu}) \to 0$ and $(\widehat{\mathbf{q}} \cdot \boldsymbol{\nu}) \to 0$ as $\omega_\mathrm{t} \to \infty$. As a result, we obtain an approximation of the Laplace–deRham operator for finite ω_t by

$$\begin{aligned} \int_{\mathcal{S}} \langle \boldsymbol{\Delta}^{\mathrm{dR}} \mathbf{p}, \widehat{\mathbf{q}} \rangle \, \mathrm{d}\mathcal{S} &\approx \int_{\mathcal{S}} (\mathrm{div}\, \widehat{\mathbf{p}}) \, (\mathrm{div}\, \widehat{\mathbf{q}}) + (\mathrm{rot}\, \widehat{\mathbf{p}}) \, (\mathrm{rot}\, \widehat{\mathbf{q}}) \, \mathrm{d}\mathcal{S} \\ &= \int_{\mathcal{S}} \underbrace{-\left[\mathrm{grad}\, (\mathrm{div}\, \widehat{\mathbf{p}}) + \mathrm{rot}\, (\mathrm{rot}\, \widehat{\mathbf{p}})\right]}_{= \widehat{\boldsymbol{\Delta}}^{\mathrm{dR}} \widehat{\mathbf{p}}} \cdot \widehat{\mathbf{q}} \, \mathrm{d}\mathcal{S}. \end{aligned} \tag{58}$$

A brief numerical study justifying this approach is found in "Appendix C." With this established, we formulate the extended weak surface Frank–Oseen energy for $\widehat{\mathbf{p}} \in H^{\mathrm{DR}}(\mathcal{S};\, \mathbb{R}^3)$ as:

$$\begin{aligned} F^{\mathcal{S}}_{\omega_\mathrm{n}, \omega_\mathrm{t}}[\widehat{\mathbf{p}}] = &\int_{\mathcal{S}} \frac{K}{2} \left[(\mathrm{div}\, \widehat{\mathbf{p}})^2 + (\mathrm{rot}\, \widehat{\mathbf{p}})^2 + \| \mathcal{B} \cdot \widehat{\mathbf{p}} \|^2 \right] \mathrm{d}\mathcal{S} \\ &+ \int_{\mathcal{S}} \frac{\omega_\mathrm{n}}{4} \left(\| \widehat{\mathbf{p}} \|^2 - 1 \right)^2 + \frac{\omega_\mathrm{t}}{2} \, (\widehat{\mathbf{p}} \cdot \boldsymbol{\nu})^2 \, \mathrm{d}\mathcal{S}. \end{aligned} \tag{59}$$

A straightforward first variation of the energy leads to the associated equation

$$\partial_t \widehat{\mathbf{p}} + K \left(\widehat{\boldsymbol{\Delta}}^{\mathrm{dR}} \widehat{\mathbf{p}} + \mathcal{B}^2 \widehat{\mathbf{p}} \right) + \omega_\mathrm{t} \, (\boldsymbol{\nu} \cdot \widehat{\mathbf{p}}) \, \boldsymbol{\nu} + \omega_\mathrm{n} \left(\| \widehat{\mathbf{p}} \|^2 - 1 \right) \widehat{\mathbf{p}} = 0 \text{ in } \mathcal{S} \times (0, \infty) \tag{60}$$

with the initial condition $\widehat{\mathbf{p}}(t = 0) = \mathbf{p}^0 \in \mathsf{T}\mathcal{S}$. Using the vector space property of the extended variational space $H^{\mathrm{DR}}(\mathcal{S};\, \mathbb{R}^3)$, we split the vector-valued variational problem into a set of componentwise scalar variational problems[2]. Therefore, let $\widehat{\mathbf{q}}$ be decomposed as

$$H^{\mathrm{DR}}(\mathcal{S};\, \mathbb{R}^3) \supseteq \left[H^1(\mathcal{S}) \right]^3 \ni \widehat{\mathbf{q}} = \sum_{i=1}^{3} \widehat{\mathrm{q}}_i \mathbf{e}_i, \quad \widehat{\mathrm{q}}_i \in H^1(\mathcal{S}), \tag{61}$$

with $\{\mathbf{e}_i\}_i$ the Euclidean basis of $\mathbb{R}^3$. We obtain a set of coupled variational problems for $\widehat{p}_i \in L^2(0, \infty;\, H^1(\mathcal{S}))$

$$\begin{aligned} &\int_{\mathcal{S}} \partial_t \widehat{\mathrm{p}}_i \widehat{\mathrm{q}} \, \mathrm{d}\mathcal{S} + \int_{\mathcal{S}} K \left[(\mathrm{div}\, \widehat{\mathbf{p}}) \, (\mathrm{grad}\, \widehat{\mathrm{q}})_i + (\mathrm{rot}\, \widehat{\mathbf{p}}) \, (\mathrm{rot}(\widehat{\mathrm{q}}\, \mathbf{e}_i)) + \left(\mathcal{B}^2 \cdot \widehat{\mathbf{p}} \right)_i \widehat{\mathrm{q}} \right] \mathrm{d}\mathcal{S} \\ &+ \int_{\mathcal{S}} \omega_\mathrm{t} \, (\boldsymbol{\nu} \cdot \widehat{\mathbf{p}}) \, \nu_i \widehat{\mathrm{q}} + \omega_\mathrm{n} \left(\| \widehat{\mathbf{p}} \|^2 - 1 \right) \widehat{\mathrm{p}}_i \widehat{\mathrm{q}} \, \mathrm{d}\mathcal{S} = 0, \quad \forall \, \widehat{\mathrm{q}} \in H^1(\mathcal{S}) \; \forall \, t \in (0, \infty) \end{aligned} \tag{62}$$

[2] Here, we use lower indices to denote the components of a vector, not to mix up with the covariant indices used in the context of differential geometry.

for $i = 1, \dots, 3$. To solve this set of variational problems, we have implemented the time discretization as in Sect. 4.1. The tangential penalty term is evaluated at the new time step t_{k+1}, and the nonlinear term is linearized using the expression f^{Taylor}. For the discretization in space, we apply the surface finite element method for scalar-valued PDEs (Dziuk 1988; Dziuk and Elliott 2007a, b) for each component. Therefore, the surface $\mathcal{S}$ is discretized by a conforming triangulation $\mathcal{S}_h$, given as the union of simplices in a simplicial complex, i.e.,

$$\mathcal{S}_h := \bigcup_{\sigma \in \mathcal{K}} \sigma.$$

We use globally continuous, piecewise linear Lagrange elements

$$\mathbb{V}_h(\mathcal{S}_h) = \left\{ v_h \in C^0(\mathcal{S}_h) \,:\, v_h|_T \in \mathbb{P}^1,\ \forall\, T \in \mathcal{T} \right\}$$

as trial and test space for all components $\widehat{\mathrm{p}}_i$ of $\widehat{\mathbf{p}}$, with $\mathcal{T}$ the set of triangular faces.

The resulting discrete problem reads: For $k = 0, 1, 2, \dots$ find $\widehat{\mathrm{p}}_i^{k+1} \in \mathbb{V}_h(\mathcal{S}_h)$ s.t.

$$\begin{aligned}
&\frac{1}{\tau_k} \int_{\mathcal{S}_h} \widehat{\mathrm{p}}_i^{k+1} \widehat{\mathrm{q}}\, \mathrm{d}\mathcal{S} + K \int_{\mathcal{S}_h} \operatorname{div} \widehat{\mathbf{p}}^{k+1} \left(\operatorname{grad} \widehat{\mathrm{q}}\right)_i + \operatorname{rot} \widehat{\mathbf{p}}^{k+1} \operatorname{rot}(\widehat{\mathrm{q}} \mathbf{e}_i) + \left(\mathcal{B}^2 \cdot \widehat{\mathbf{p}}\right)_i \widehat{\mathrm{q}}\, \mathrm{d}\mathcal{S} \\
&\quad + \omega_{\mathrm{t}} \int_{\mathcal{S}_h} \boldsymbol{\nu} \cdot \widehat{\mathbf{p}}^{k+1} \nu_i \widehat{\mathrm{q}}\, \mathrm{d}\mathcal{S} + \omega_{\mathrm{n}} \int_{\mathcal{S}_h} \left(\|\widehat{\mathbf{p}}^k\|^2 - 1 \right) \widehat{\mathrm{p}}_i^{k+1} \widehat{\mathrm{q}} + 2 \widehat{\mathrm{p}}_i^k \widehat{\mathbf{p}}^k \cdot \widehat{\mathbf{p}}^{k+1} \widehat{\mathrm{q}}\, \mathrm{d}\mathcal{S} \\
&= \frac{1}{\tau_k} \int_{\mathcal{S}_h} \widehat{\mathrm{p}}_i^k \widehat{\mathrm{q}}\, \mathrm{d}\mathcal{S} + 2\omega_{\mathrm{n}} \int_{\mathcal{S}_h} \|\widehat{\mathbf{p}}^k\|^2 \widehat{\mathrm{p}}_i^k \widehat{\mathrm{q}}\, \mathrm{d}\mathcal{S}, \quad \forall\, \widehat{\mathrm{q}} \in \mathbb{V}_h(\mathcal{S}_h)
\end{aligned} \tag{63}$$

for $i = 1, \dots, 3$. To assemble and solve the resulting system, we use the FEM toolbox AMDiS (Vey and Voigt 2007; Witkowski et al. 2015) with domain decomposition on eight processors. As linear solver, we have used a restarted GMRES method with a restart cycle of 30, modified Gram–Schmidt orthogonalization, and a block Jacobi preconditioner with ILU(0) local solver on each partition.

4.5 Diffuse Interface Approximation

Based on the penalty formulation, described in Sect. 4.4, we formulate a diffuse interface approximation following the general treatment introduced in Rätz and Voigt (2006). We use a simple (e.g., box like) embedding domain $\mathcal{S} \subset \Omega \subset \mathbb{R}^3$ and describe the surface as the $1/2$ level set of a phase-field variable ϕ defined on Ω:

$$\phi(\mathbf{x}) = \frac{1}{2} \left(1 - \tanh\left(\frac{3}{\varepsilon} d_{\mathcal{S}}(\mathbf{x}) \right) \right), \tag{64}$$

with interface thickness ε and $d_{\mathcal{S}}(\mathbf{x})$ a signed-distance function. This gives an approximation of the surface delta function

$$\delta_{\mathcal{S}} \simeq \frac{36}{\varepsilon} \phi^2 (\phi - 1)^2 = W(\phi). \tag{65}$$

In this diffuse interface framework, we consider vector fields $\widetilde{\mathbf{p}} : \Omega \to \mathsf{T}\mathbb{R}^3$ extended from the surface to the embedding domain Ω. The outward pointing surface normals are extended smoothly to Ω by using $\widetilde{\boldsymbol{\nu}} = \nabla\phi/\|\nabla\phi\|$, and the shape operator in the embedding domain is defined in terms of this extended normal, i.e., $\widetilde{\mathcal{B}}_{ij} = -\left[\pi_{\mathsf{T}\mathcal{S}}\nabla\widetilde{\boldsymbol{\nu}}_j\right]_i$.

Considering the diffuse interface approximation of the extended weak surface Frank–Oseen energy

$$\begin{aligned} F^{\Omega}_{\omega_{\mathrm{n}},\omega_{\mathrm{t}}}[\widetilde{\mathbf{p}}] = &\int_\Omega \frac{K}{2} W(\phi)\left[(\operatorname{div}\widetilde{\mathbf{p}})^2 + (\operatorname{rot}\widetilde{\mathbf{p}})^2 + \|\widetilde{\mathcal{B}}\cdot\widetilde{\mathbf{p}}\|^2\right]\mathrm{d}\mathcal{S} \\ &+ \int_\Omega \frac{\omega_{\mathrm{n}}}{4} W(\phi)\left(\|\widetilde{\mathbf{p}}\|^2 - 1\right)^2 + \frac{\omega_{\mathrm{t}}}{2} W(\phi)\,(\widetilde{\mathbf{p}}\cdot\widetilde{\boldsymbol{\nu}})^2\,\mathrm{d}\mathcal{S} \end{aligned} \tag{66}$$

with $\widetilde{\mathbf{p}} \in H^{\mathrm{DR}}(\Omega;\ \mathbb{R}^3)$, we obtain, by straightforward first variation, the L^2-gradient flow formulation

$$W(\phi)\partial_t\widetilde{\mathbf{p}} + K\,\widetilde{\boldsymbol{\Delta}}^{\mathrm{dR}}\widetilde{\mathbf{p}} + W(\phi)\left[K\left(\widetilde{\mathcal{B}}^2\cdot\widetilde{\mathbf{p}}\right) + \omega_{\mathrm{t}}\,(\widetilde{\boldsymbol{\nu}}\cdot\widetilde{\mathbf{p}})\,\widetilde{\boldsymbol{\nu}} + \omega_{\mathrm{n}}\left(\|\widetilde{\mathbf{p}}\|^2 - 1\right)\widetilde{\mathbf{p}}\right] = 0 \tag{67}$$

in $\Omega\times(0,\infty)$. Here, we have introduced the diffuse interface Laplace–deRham operator $\widetilde{\boldsymbol{\Delta}}^{\mathrm{dR}}$ by

$$\widetilde{\boldsymbol{\Delta}}^{\mathrm{dR}}\widetilde{\mathbf{p}} := -\left[\nabla\left(W(\phi)\nabla\cdot\widetilde{\mathbf{p}}\right) + \widetilde{\boldsymbol{\nu}}\times\nabla\left(W(\phi)\nabla\cdot(\widetilde{\mathbf{p}}\times\widetilde{\boldsymbol{\nu}})\right)\right]. \tag{68}$$

As initial condition, we set $\widetilde{\mathbf{p}}(t=0) = \widetilde{\mathbf{p}}^0$ in Ω such that $\widetilde{\mathbf{p}}^0|_{\mathcal{S}} = \mathbf{p}^0$. As boundary condition, we specify

$$\nabla\widetilde{\mathrm{p}}_i\cdot\mathbf{n} = 0, \quad \text{on } \partial\Omega\times(0,\infty),$$

for $i = 1,\dots,3$, where $\mathbf{n}$ denotes the outward pointing normal of $\partial\Omega$. For Ω big enough, the condition on the outer boundary does not influence the solution on the surface. Finally, we obtain a set of coupled variational problems for $\widetilde{p}_i \in L^2(0,\infty;\ H^1(\Omega))$

$$\begin{aligned} &\int_\Omega W(\phi)\partial_t\widetilde{\mathrm{p}}_i\widetilde{\mathrm{q}}\,\mathrm{d}V \\ &\quad + \int_\Omega K\,W(\phi)\left[(\nabla\cdot\widetilde{\mathbf{p}})\,\partial_i\widetilde{\mathrm{q}} + \nabla\cdot(\widetilde{\mathbf{p}}\times\widetilde{\boldsymbol{\nu}})\,\nabla\cdot(\widetilde{\mathrm{q}}\mathbf{e}_i\times\widetilde{\boldsymbol{\nu}}) + \left(\widetilde{\mathcal{B}}^2\cdot\widetilde{\mathbf{p}}\right)_i\widetilde{\mathrm{q}}\right]\mathrm{d}V \\ &\quad + \int_\Omega \omega_{\mathrm{t}}W(\phi)\,(\widetilde{\boldsymbol{\nu}}\cdot\widetilde{\mathbf{p}})\,\widetilde{\nu}_i\widetilde{\mathrm{q}} + \omega_{\mathrm{n}}W(\phi)\left(\|\widetilde{\mathbf{p}}\|^2 - 1\right)\widetilde{\mathrm{p}}_i\widetilde{\mathrm{q}}\,\mathrm{d}V \\ &= 0 \quad \forall\,\widetilde{\mathrm{q}}\in H^1(\Omega)\ \forall\,t\in(0,\infty), \end{aligned} \tag{69}$$

for $i = 1,\dots,3$.

The definition of $\widetilde{\boldsymbol{\Delta}}^{\mathrm{dR}}$ in (68) is motivated by the componentwise formulation of $\widehat{\boldsymbol{\Delta}}^{\mathrm{dR}}$ in combination with the diffuse approximations of surface differential operators

for scalar functions $f : \mathcal{S} \to \mathbb{R}$ with smooth extension $\widetilde{f} : \Omega \to \mathbb{R}$. In this framework, we have the following convergence results:

$$\begin{aligned}
\lim_{\varepsilon\to 0}\int_\Omega W(\phi)\widetilde{f}\,\widetilde{\mathrm{q}}\,\mathrm{d}V &= \int_{\mathcal{S}} f\,\widetilde{\mathrm{q}}\,\mathrm{d}\mathcal{S},\\
\lim_{\varepsilon\to 0}\int_\Omega W(\phi)\partial_i\widetilde{f}\,\widetilde{\mathrm{q}}\,\mathrm{d}V &= \int_{\mathcal{S}} (\operatorname{grad} f(\mathbf{x}))_i\,\widetilde{\mathrm{q}}\,\mathrm{d}\mathcal{S},\\
\lim_{\varepsilon\to 0}\int_\Omega \nabla\cdot\left(W(\phi)\nabla\widetilde{f}\right)\widetilde{\mathrm{q}}\,\mathrm{d}V &= \int_{\mathcal{S}} \operatorname{div}(\operatorname{grad} f)\,\widetilde{\mathrm{q}}\,\mathrm{d}\mathcal{S},
\end{aligned}$$

for $\widetilde{\mathrm{q}} \in H^1(\Omega)$, see Rätz and Voigt (2007). A regularization is added to the function $W(\phi)$ in some of the terms, to allow for a more stable solution of the linear system: $W_\zeta(\phi) := \max(W(\phi), \zeta)$ with $\zeta \ll 1$. This regularization is justified in Rätz and Voigt (2006), Li et al. (2009).

Applying a standard finite element method with globally continuous, piecewise linear elements $\mathbb{V}_h(\Omega_h) = \{v_h \in C^0(\Omega_h) \ : \ v_h|_T \in \mathbb{P}^1, \ \forall\, T \in \Omega_h\}$ on a triangulation Ω_h of Ω, the time discretization as above and inserting the regularized delta function approximation W_ζ, results in a sequence of diffuse interface problems: For $k = 0, 1, \ldots$, find $\widetilde{\mathrm{p}}_i^{k+1} \in \mathbb{V}_h(\Omega)$ s.t.

$$\begin{aligned}
&\frac{1}{\tau_k}\int_{\Omega_h} W_\zeta(\phi)\widetilde{\mathrm{p}}_i^{k+1}\widetilde{\mathrm{q}}\,\mathrm{d}V\\
&\quad + K\int_{\Omega_h} W_\zeta(\phi)\nabla\cdot\widetilde{\mathbf{p}}^{k+1}\partial_i\widetilde{\mathrm{q}}\\
&\quad + W(\phi)\left[\nabla\cdot\left(\widetilde{\mathbf{p}}^{k+1}\times\widetilde{\boldsymbol{\nu}}\right)\nabla\cdot(\mathbf{e}_i\widetilde{\mathrm{q}}\times\widetilde{\boldsymbol{\nu}}) + \left(\widetilde{\mathcal{B}}^2\cdot\widetilde{\mathbf{p}}\right)_i\widetilde{\mathrm{q}}\right]\mathrm{d}V\\
&\quad + \omega_{\mathrm{t}}\int_{\Omega_h} W(\phi)\widetilde{\boldsymbol{\nu}}\cdot\widetilde{\mathbf{p}}^{k+1}\widetilde{\nu}_i\widetilde{\mathrm{q}}\,\mathrm{d}V\\
&\quad + \omega_{\mathrm{n}}\int_{\Omega_h} W(\phi)\left[\left(\|\widetilde{\mathbf{p}}^k\|^2-1\right)\widetilde{\mathrm{p}}_i^{k+1} + 2\widetilde{\mathrm{p}}_i^k\widetilde{\mathbf{p}}^k\cdot\widetilde{\mathbf{p}}^{k+1}\right]\widetilde{\mathrm{q}}\,\mathrm{d}V\\
&= \frac{1}{\tau_k}\int_{\Omega_h} W_\zeta(\phi)\widetilde{\mathrm{p}}_i^k\widetilde{\mathrm{q}}\,\mathrm{d}V + 2\omega_{\mathrm{n}}\int_{\Omega_h} W(\phi)\|\widetilde{\mathbf{p}}^k\|^2\widetilde{\mathrm{p}}_i^k\widetilde{\mathrm{q}}\,\mathrm{d}V, \quad \forall\,\widetilde{\mathrm{q}}\in\mathbb{V}_h(\Omega), \qquad (70)
\end{aligned}$$

for $i = 1, \ldots, 3$, with $\widetilde{\mathbf{p}}^0$ a smooth extension[3] of $\mathbf{p}^0$ to the domain Ω. To assemble and solve the resulting system, we use the FEM toolbox AMDiS (Vey and Voigt 2007; Witkowski et al. 2015) with domain decomposition on 64 processors. As linear solver, we have used a restarted GMRES method with a restart cycle of 30, modified Gram–Schmidt orthogonalization, and a block Jacobi preconditioner with ILU(0) local solver on each partition, as above for the sFEM method.

[3] A smooth extension to the domain Ω is implemented by successively extending fields to its surroundings, utilizing (15), until the whole domain is covered, see also Stöcker (2008).

4.6 Surface Approximation and Grids

Surfaces similar to a sphere $\mathbb{S}^2$ can be triangulated by projecting a triangulation of the sphere to $\mathcal{S}$, utilizing the coordinate projection π. For the DEC method, this triangulation must be well centered; in other words, the circumcenter of each surface triangle must be located within the triangle. This property can be realized by triangles with internal angle less than 90°. An iterative procedure is applied to the projected sphere triangulation to fulfill this requirement, by shifting points tangentially to the surface so that all triangles have nearly equal internal angles and edge lengths. The algorithm is described in Nitschke (2014).

Other surfaces may be triangulated by cutting tetrahedra at the zero-level set of an implicit surface description. This triangulation must be optimized by retriangulation, e.g., by using (Valette et al. 2008, 2014), and utilizing additionally the iterative procedure to get a well-centered complex, as above. Recently, an algorithm for mesh optimization, based on an edge collapsing strategy, was implemented in Stenger (2016). Even if sFEM would need less requirements on the surface mesh, we use the same meshes as for DEC. We have chosen a grid width h, i.e., the maximal radius of all triangles, to be approximately one-sixth of the defect core radius that is estimated experimentally.

For DI we use a 3D conformal tetrahedral mesh adaptively refined near the surface. Therefore, the interfacial region, i.e., $\{\mathbf{x} \in \Omega : \phi(\mathbf{x}) \in [0.1, 0.9]\}$, contains approximately 7 grid points in normal direction to the surface. This refinement guarantees good agreement with the sharp surface limit, see, e.g., Aland et al. (2010), Aland et al. (2013) for a justification and quantitative study. The signed-distance function, the phase field is based on, is calculated from the triangulated surface by an algorithm utilizing a ray tracing principle. For every grid point in the 3D mesh, the distance to the surface is calculated, and afterward, the correct sign is assigned. This algorithm is explained and implemented in Stenger (2016) and has an asymptotic complexity of $\sim \mathcal{O}(|\Omega_h| \cdot \log |\mathcal{T}|)$.

5 Computational Results

We validate the proposed approaches on the unit sphere. Due to lack of analytical description of minimizers $\mathbf{p} \in H^{\mathrm{DR}}(\mathcal{S}; \mathsf{T}\mathcal{S})$, we compare the numerical results with each other. The DEC approach thereby serves as reference. We also explore the stability of minimal energy defect configurations on more complicated surfaces with non-constant curvature and demonstrate the tight interplay of defect localization and geometric properties. Within these studies, we show the possibility of equilibrium states other than the trivial realization of the Poincaré–Hopf theorem and thus the possibility to reduce the weak surface Frank–Oseen energy by incorporating additional defects. To validate these results, we again compare the numerical results with each other. The penalty parameter ω_{n} is chosen, such that the defect core radius is resolved, see Table 2. The section is concluded by providing information on the numerical effort for each method.

Table 2 Simulation parameters for the two setups: relaxation on the sphere and nonic surface

		Sphere	Nonic surface
Time	t_{end}	5	Variable [a]
	$\tau_k \equiv \tau$	10^{-3}	$5 \cdot 10^{-4}$
Model	K	1	1
	ω_{n}	10^3	200
	ω_{t}	$[10^3 - 10^5]$	10^5
SPH	N	190	–
	N_θ	250	–
	N_φ	400	–
	τ	2×10^{-4}	–
sFEM	h	0.013	0.035
DI	ε	0.15	0.2
	ζ	10^{-6}	10^{-6}
	h	0.023	0.078
	Ω	$[-1.5, 1.5]^3$	$[-2, 3] \times [-2, 2]^2$

[a]The end time of the simulation is chosen so that the system is close to equilibrium, i.e., if the criterion $|F(t_{k+1}) - F(t_k)| < 10^{-14} \cdot |F(t_{k+1})|$ is fulfilled

5.1 Method Comparison on Sphere

We consider an initial condition $\mathbf{p}^0$ with two sinks (✳ $+1$), a source (✳ $+1$) and a saddle (✳ -1) on the unit sphere $\mathcal{S} = \mathbb{S}^2$. The numbers are the topological charges or the winding numbers $\text{ind}_V(\mathbf{d}_i)$ of the defects $\mathbf{d}_i$. They are defined as the algebraic sum of the number of revolution of $\mathbf{p}$ along a small counterclockwise oriented curve around the defect. The Poincaré–Hopf theorem requires

$$\sum_i \text{ind}_V(\mathbf{d}_i) = \chi(\mathcal{S}), \tag{71}$$

which in the present case is satisfied as $1+1+1-1 = 2$. The four defects are positioned equidistant on the x–y-equatorial plane. To avoid metastable configurations, we shift one sink defect slightly closer to the saddle point defect.

$$\mathbf{p}^0 = \frac{\pi_{\mathsf{T}\mathcal{S}}\hat{\mathbf{p}}^0}{\|\pi_{\mathsf{T}\mathcal{S}}\hat{\mathbf{p}}^0\|}, \quad \text{where}$$
$$\hat{\mathbf{p}}^0 = \begin{cases} [-x, 0, -z]^{\mathrm{T}} & |y| \geq \cos\frac{\pi}{4} \\ [0, y, z]^{\mathrm{T}} & x \geq \cos\frac{\pi}{4} \\ [0, \sin(\pi\,(y-\lambda)), -\sin(\pi z)]^{\mathrm{T}} & x \leq -\cos\frac{\pi}{4} \\ \left[\left|\frac{y}{\cos\frac{\pi}{4}}\right| - 1, \frac{y}{\cos\frac{\pi}{4}}, 0\right]^{\mathrm{T}} & \text{otherwise} \end{cases} \tag{72}$$

with $\lambda = 0.01$ used in our simulations.

Since opposing topological charges attract each other, we observe the motion of the two sink defects to the saddle point defect and eventually the fusion of the saddle point defect with the closer sink defect (see Fig. 1). The time needed for the annihilation

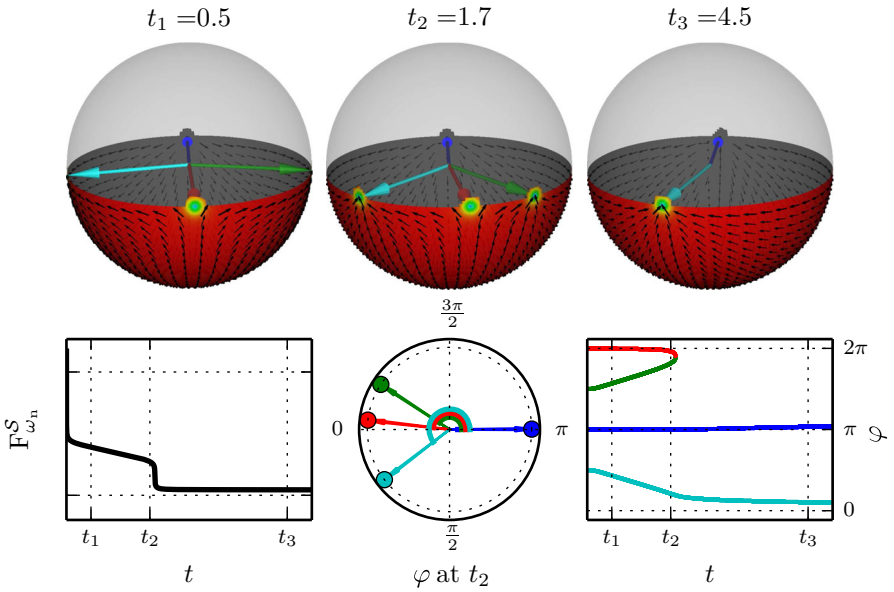

Fig. 1 *Top* sequence of director field configurations (*glyphs*) and defect positions (*color gradient* on surface and *large arrows*) in the evolution of the four-defect test case, at time t_0, the four-defect configuration, time t_1, the defect annihilation, and time t_2, the two-defect configuration. *Bottom* energy evolution (*left*), defect positions in x–y-equatorial plane at t_2 (*middle*) and defect trajectories of the four-defect test case (*right*). The angle $\varphi \in [0, 2\pi)$ describes the defect positions in the x–y-equatorial plane. *Colors* of the defects: source (*dark blue*), sinks (*cyan* and *green*), saddle point (*red*) (Color figure online)

of the two defects is denoted by t_f and called fusion time. Finally, the remaining two defects relax to a position with maximal distance. Due to the symmetry of the setup, the defect positions will remain in the equatorial plane.

These dynamics are consistently observed within all methods. To measure deviations in the proposed numerical methods, we compare against the DEC solution. Therefore, we introduce as quantitative measure a density like mean energy error ϵ_e (normalized by the area A of the surface, $A_{\mathbb{S}^2} = 4\pi$) and as qualitative measure the error in the defect fusion time ϵ_f,

$$\epsilon_\mathrm{e} := \frac{1}{A\, t_\mathrm{end}} \int_0^{t_\mathrm{end}} \left| \frac{F^{\mathcal{S}(\Omega)}_{\omega_\mathrm{n},(\omega_\mathrm{t})}(\mathsf{M}) - F^{\mathcal{S}}_{\omega_\mathrm{n}}(\mathsf{DEC})}{F^{\mathcal{S}}_{\omega_\mathrm{n}}(\mathsf{DEC})} \right| \mathrm{d}t, \tag{73}$$

$$\epsilon_\mathrm{f} := \left| \frac{t_\mathrm{f}(\mathsf{M}) - t_\mathrm{f}(\mathsf{DEC})}{t_\mathrm{f}(\mathsf{DEC})} \right|, \tag{74}$$

for a numerical method M. Within this framework, we evaluate the proposed vector-valued methods DEC and SPH, and the componentwise methods sFEM and DI, with parameters from Table 2.

Figure 2 shows the obtained error measures. The methods essentially show matching solutions. The relative energy difference and difference in defect fusion time is reduced

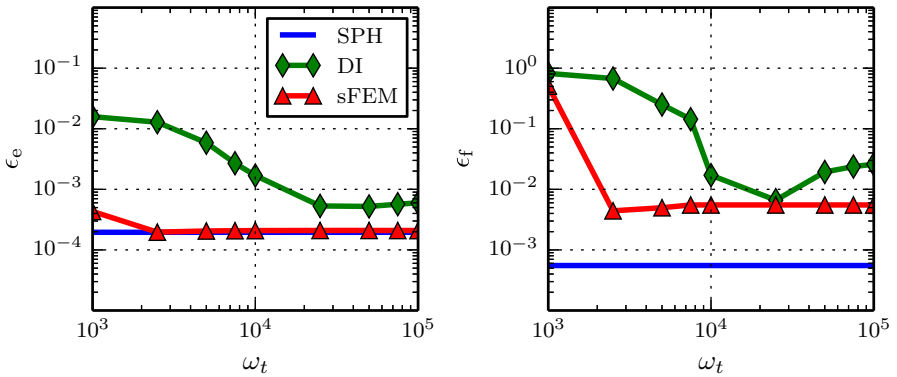

Fig. 2 The errors in mean energy ϵ_e (*left*) and fusion time of defects ϵ_f (*right*) for various tangentiality penalty parameters ω_t. Three different methods are compared to DEC: spherical harmonics (*blue*), parametric FEM (*red*), and diffuse interface (*green*) (Color figure online)

for increasing penalty factor ω_t, but is limited by the differences in the compared methods, e.g., difference in the location of DOFs and the discretization of the surface. The SPH method does not depend on a tangentiality penalization as the DEC method. Thus, the error values result from a difference in the surface representation and the truncation in the spherical harmonics expansion. Apart from this, two qualitatively different behaviors for sFEM and DI can be observed. Where the method sFEM shows nearly constant errors (at least for $\omega_t > 2500$), the method DI shows a dependence on the penalty parameter. This effect arises form the interaction of the penalty forcing and the geometric approximation of $\mathcal{S}$ by a smeared-out delta function, i.e., a non-constant penalty factor throughout the interface. Close to the surface, the director field $\tilde{\mathbf{p}}$ is not guaranteed to be tangential to $\mathcal{S}$ for ω_t too small. Increasing the penalty factor finally leads to tangential fields in the surrounding of the interface. This results in error values close to those of sFEM. A difference in these two methods is expected, due to the additional approximation of the surface and the surface differential operators by the diffuse interface representation.

Within a reasonable tolerance, all four methods show the same dynamic behavior along quantitative and qualitative error measures and converge to the same stationary solution with two defects, a source (+1) and a sink (+1), which are at maximal distance from each other.

5.2 Higher-Order Surfaces

To further validate the consistency of the methods DEC, sFEM and DI, we extend the test setup to a sequence of surfaces with non-constant curvature, see Fig. 3 for examples. All surfaces have $\chi(\mathcal{S}) = 2$, thus allowing defect configurations as in the previous example.

The construction of the surfaces is based on a deformation of the unit sphere, such that regions with positive and negative Gaussian curvature emerge. Our goal is to study the influence of these regions on the defect location. Are defects attracted by

$C = 0.5$ $C = 0.635$ $C = 1.175$

Fig. 3 Nonic surfaces corresponding to three different stretching parameters C. *Left* surface with defect fusion time > 0. *Center* four-defect configuration gets stable. *Right* four-defect configuration is energetically equivalent to two-defect configuration

these regions? Is there a relation between the topological charge of the defect and the Gaussian curvature?

The postulated parametrization of the unit sphere $\mathbb{S}^2$, $\mathbf{x}_{\mathbb{S}^2}(\theta, \varphi)$, given in Sect. 4.3, is stretched in z-direction by the displacement function $f_{C,r}$ with factors $r \in (0, 1)$ and $C > 0$,

$$f_{C,r}(z) := \frac{1}{4} C z^2 \left[(z+1)^2 (4 - 3z) + r(z-1)^2 (4 + 3z) \right]$$

and compress along y-direction by a factor $B \in [0, 1)$. This leads to the parametrization

$$\mathbf{x}(\theta, \varphi) := \mathbf{x}_{\mathbb{S}^2}(\theta, \varphi) + f_{C,r}(\cos\theta)\, \mathbf{e}^x - B \sin\theta \sin\varphi\, \mathbf{e}^y. \tag{75}$$

The surface can also be expressed implicitly by the zero-level set of the function

$$\varrho(x, y, z) := \big(x - f_{C,r}(z)\big)^2 + \frac{1}{(1-B)^2} y^2 + z^2 - 1. \tag{76}$$

This gives a polynomial ϱ of degree 10, which motivates the name *nonic surfaces*. The asymmetry of the surfaces w.r.t. the x-z-plane prevents metastable defects configurations. The necessary surface quantities can be derived directly from the level set formulation by $\widetilde{\boldsymbol{\nu}} = \nabla\varrho / \|\nabla\varrho\|$ and $\mathcal{B}_{ij} = -\left[\pi_{\mathsf{T}\mathcal{S}} \nabla \widetilde{\boldsymbol{\nu}}_j\right]_i$.

To investigate the energy value $F^{\mathcal{S}}_{\omega_n}[\mathbf{p}^*]$ of a stationary solution $\mathbf{p}^*$ and the stability of defect configurations, we analyze the evolution of two different initial solutions $\mathbf{p}^0_{(4)}$ and $\mathbf{p}^0_{(2)}$. The first one, $\mathbf{p}^0_{(4)}$, has four separated defects, while the second one, $\mathbf{p}^0_{(2)}$, has two.

At first, we consider the projected unit vector $\mathbf{e}^x$, which can be represented by the surface gradient of the x-coordinate, i.e.,

$$\mathbf{p}^0_{(4)} := \pi_{\mathsf{T}\mathcal{S}}\, \mathbf{e}^x = \operatorname{grad} x = (\mathbf{d}x)^\sharp. \tag{77}$$

On an edge $e = [v_1, v_2] \in \mathcal{E}$, where the face $T_1 \succ e$ is right of e and $T_2 \succ e$ is left of e, so that $\star e = [c(T_1), c(e)] + [c(e), c(T_2)]$ is the dual edge, we can approximate the

1-form $\mathbf{d}x$, utilizing integration by parts on e, by

$$\underline{\boldsymbol{\alpha}}^0_{(4)}(e) = \left(v_2^x - v_1^x, -\frac{|e|}{|\star e|} \left([c(T_2)]^x - [c(T_1)]^x \right) \right). \tag{78}$$

To enforce a two-defect solution in equilibrium for the second case, we project a slightly rotated unit vector $\mathbf{e}^y$ to the surface. The rotation by an angle γ in the normal plane of the $\mathbb{R}^3$-vector $[-1, 0, 1]^T$ is thereby represented by the rotation matrix R_γ. This defines

$$\mathbf{p}^0_{(2)} := \pi_{\mathsf{T}\mathcal{S}} R_\gamma \, \mathbf{e}^y. \tag{79}$$

Our choice of γ is 0.05. In the context of DEC, the evaluation of a vector field $\mathbf{q} \in \mathsf{T}\mathcal{S}$ with the dual edge vector $\mathbf{e}_\star$ on edge e at the intersection $e \cap \star e = c(e)$ is ambiguous. To overcome this, we define in a canonical way a dual 1-chain, utilizing the definition of a dual edge $\star e = \star e|_{T_1} + \star e|_{T_2}$. This leads to

$$\mathbf{q}(c(e)) \cdot \mathbf{e}_\star := \mathbf{q}(c(e)) \cdot \left(\mathbf{e}_\star \big|_{T_1} + \mathbf{e}_\star \big|_{T_2} \right) = \mathbf{q}(c(e)) \cdot (c(T_2) - c(T_1)) \,,$$

where the face $T_1 \succ e$ is right of the edge e and $T_2 \succ e$ is located left. Thus, we get the initial discrete PD-1-form

$$\underline{\boldsymbol{\alpha}}^0_{(2)}(e) = \left(\mathbf{p}^0_{(2)}(c(e)) \cdot \mathbf{e}, -\frac{|e|}{|\star e|} \mathbf{p}^0_{(2)}(c(e)) \cdot \mathbf{e}_\star \right). \tag{80}$$

The normalized versions of $\mathbf{p}^0_{(i)}$ and $\underline{\boldsymbol{\alpha}}^0_{(i)}$ can easily be constructed by pointwise or edgewise normalization, respectively, using the definition of the norm in (36) for the discrete PD-1-forms.

Within this setup, we evaluate the energy for stationary solutions $\mathbf{p}^*$ and the number of defects for both initial solutions $\mathbf{p}^0_{(4/2)}$ for a sequence of values $C \in [0, 1.5]$. The parameter $r = 0.95$ remains fixed while B is related to C by $B = 7/20C$.

An example of the two different initial fields relaxed to equilibrium is shown in Fig. 4 for a specific nonic surface. We find $+1$ defects at extrema of the Gaussian curvature, while a -1 defect may appear at the saddle point. This dependency is in agreement with results for the similar problem of flow on curved surfaces (Reuther and Voigt 2015; Nitschke et al. 2016).

For shapes with $C \in [0.5, 0.635]$, we observe that both initial solutions converge to a two-defect configuration. In Fig. 5 (right), we plot the fusion time for defect annihilation for initial condition $\mathbf{p}^0_{(4)}$. Notice the steep increase in this time for $C \nearrow 0.635$. For $C \gtrsim 0.635$, a four-defect configuration becomes stable. It poses a local energetic minimum. Further increasing the parameter C, continuously amplifies the Gaussian curvature on the bulges and saddle. As shown in Fig. 5 (left), this leads to a decreasing energy cost for the four-defect stationary solution, while costs for the two-defect solution increase monotonically until the energies are equal at $C \approx 1.175$. For $C \gtrsim 1.175$, the four-defect solution becomes energetically favorable. This behavior

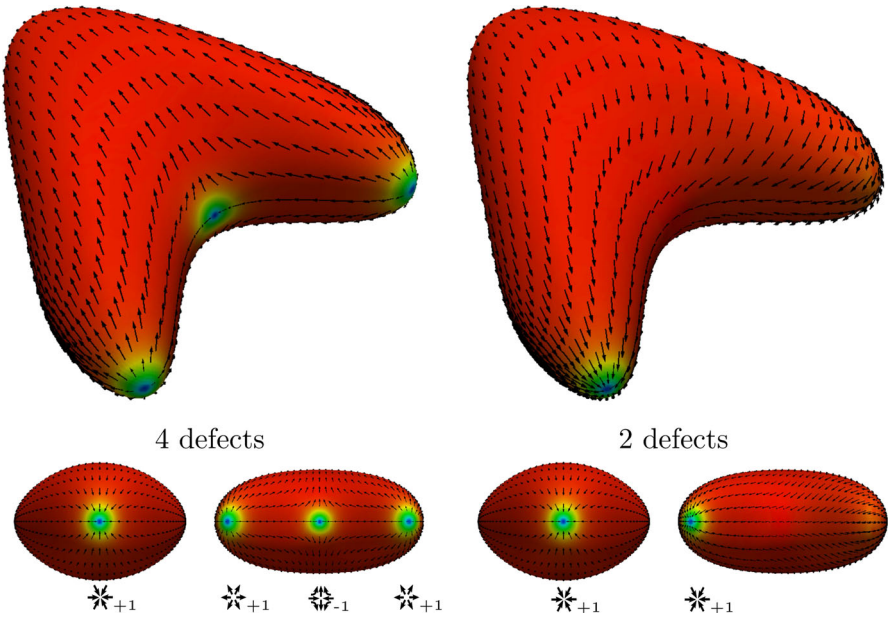

Fig. 4 Equilibrium states for surface with $C = 1.175$, norm defects (*color gradient*) and director (*glyphs*). *Second row* back and front detail of configuration (Color figure online)

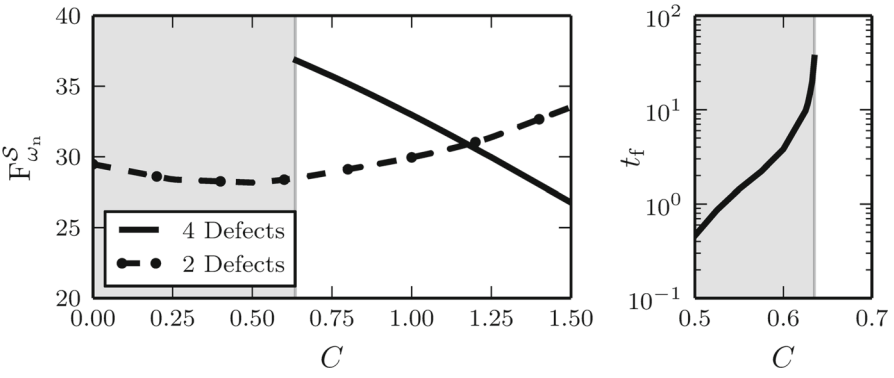

Fig. 5 Energy $F^{\mathcal{S}}_{\omega_n}$ for stationary solutions with four and two defects for nonic shapes with $C \in [0, 1.5]$ (*left*) and defect fusion time for the four-defect initial solution (*right*)

is stable against variations in the penalty parameter ω_n, which is chosen, such that the defect core radius is resolved, see Table 2.

These experiments emphasize the impact of curvature on the energetic cost of a defect configuration and prove the key role of domain geometry in enabling non-trivial realizations of the Poincaré–Hopf theorem. Figure 6 shows snapshots of the evolution on the most deformed surface with $C = 1.5$ and noise used as initial condition. Which stationary shape is selected strongly depends on the initial condition. We here only show the one converging to the four-defect configuration.

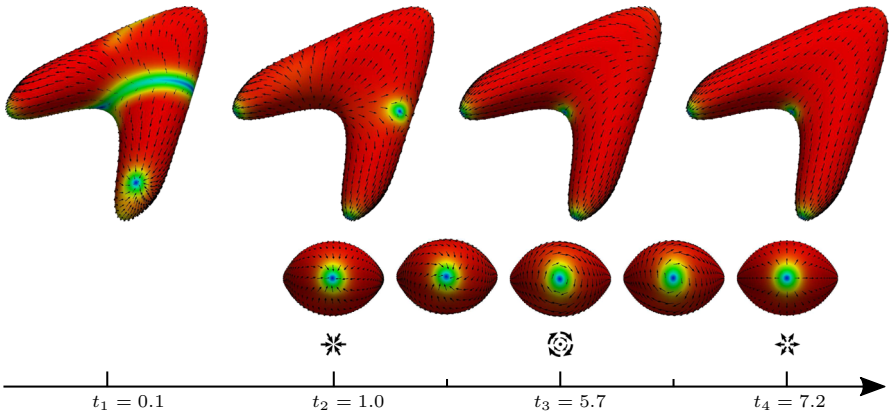

Fig. 6 Snapshots of the time evolution and the final stationary solutions with four defects on the nonic shapes with $C = 1.5$. *First row* top view. *Second row* back view with a single defect, evolution from a sink shape (at $t = 1$) over vortex shape (at $t = 5.7$) to the final source shape (at $t = 7.2$) (Color figure online)

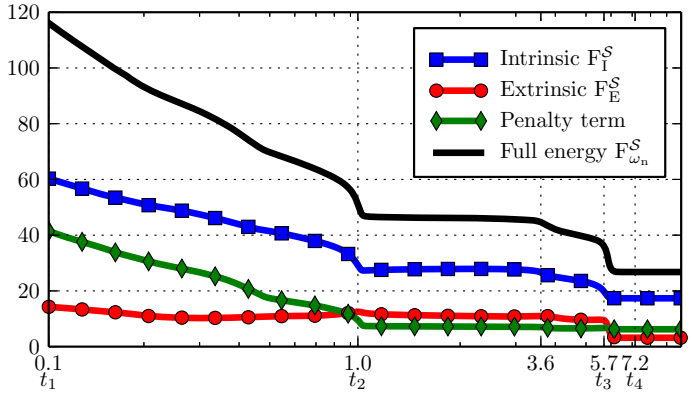

Fig. 7 Development of the energy parts in the relaxation starting from random initial state. The four parts plotted with *lines* and *symbols* sum up to the full energy $F_{\omega_n}^{\mathcal{S}}$. Highlighted are five time steps that mark changing events. From $t = 0.1$ to $t = 3.6$, the defects move to their final position. In the time period $t = 1.0$ to $t = 5.7$, the back defect rotates by 90°, from a sink to a vortex defect. From time $t = 5.7$ to $t = 7.2$, the back defect rotates further by 90°, from a vortex defect to a source defect (Color figure online)

The relaxation shows four periods with distinct behavior. Starting from a random initial configuration the noise smoothes out to a state with emerging localized defects at time around $t = 0.1$. Until time $t = 1$, these defects reach their final normalization shape; in other words, the penalization term in the energy reduces up to this time and stays constant from this time on, as shown in Fig. 7. The defects move at first slowly and then very fast to their final position around the high curvature areas and the saddle point. This happens until time $t = 3.6$. When the back defect reaches its final position, it starts to rotate the vector field up to 90°. Thus, a sink defect evolves to a vortex defect at around time $t = 5.7$. This process continues and rotates the vector

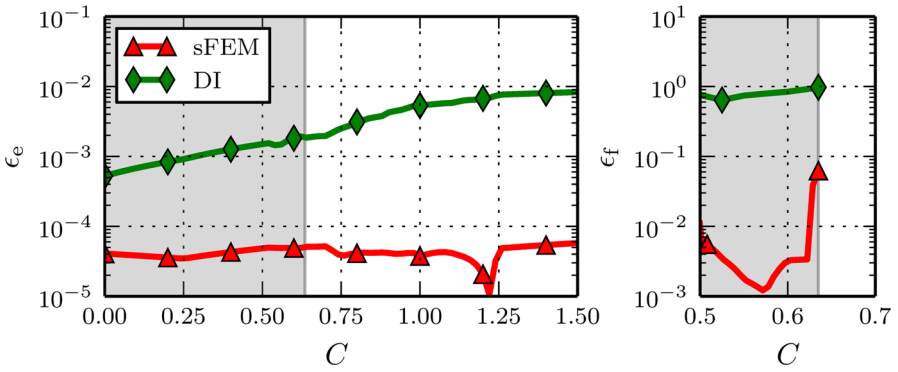

Fig. 8 Relative errors w.r.t. DEC solution of mean energy (*left*) and fusion time (*right*) for nonic shapes $C \in [0, 2]$ and the numerically methods parametric FEM (*red dashed*) and diffuse interface (*green solid*) (Color figure online)

field around this back defect further by 90° until a source defect shape is reached at around time $t = 7.2$.

Besides these exploratory results, shown in Fig. 5 we also use this parameter study to verify the quality of the numerical methods sFEM and DI. In Fig. 8, we plot the relative errors introduced in (73) for the mean energy and fusion time. As numerical parameters, we have chosen values listed in Table 2 in the column *nonic surface*.

As shown in Fig. 8 (left), we observe the same behavior with both methods, across the full range of shapes $C \in [0, 1.5]$, within reasonable error bounds. The more approximative DI yields significant stronger deviations from the DEC results, up to two orders of magnitude in the mean energy error. Furthermore, we notice increasing errors with amplified curvature. The critical point $C_{\text{crit}} = 0.635$ of emergence of a new stable defect configuration is qualitatively reproduced by both methods. DEC and sFEM yield identical results for C_{crit}, up to the probing grid spacing of $\delta C = 2.5 \cdot 10^{-3}$. DI produces a critical value of 0.7125, which corresponds to a relative error of 0.122 w.r.t. the DEC result. As a result, the dynamics evaluated by DI close to this critical event exhibit distinct deviations leading to substantial relative errors for the fusion time as shown in Fig. 8 (right).

We do not compare the dynamic evolution if started from noise, as identical initial conditions cannot be specified. However, also sFEM and DI produce evolutions which are qualitatively the same as in Fig. 6. Again, whether a two-defect or four-defect configuration is reached strongly depends on the initial condition.

5.3 Performance Comparison

We summarize pros and cons of the considered numerical methods, with respect to complexity, accuracy, generality, and numerical performance.

As a first quality measure, we consider the applicability of the methods to various geometric surfaces. Here SPH is the most restrictive as it can only be applied to spherical surfaces, since eigenfunctions and eigenvalues of the Laplace–deRham operator

Table 3 Number of degrees of freedom ♯DOFs and number of nonzeros per row of the matrix for the three methods that assemble a linear system

	DEC	sFEM	DI
♯DOFs	$2 \cdot \lvert\mathcal{E}\rvert \approx 6 \cdot \lvert\mathcal{V}\rvert$	$3 \cdot \lvert\mathcal{V}\rvert$	$\gg 3 \cdot \lvert\mathcal{V}\rvert$
NNZ/row	12	20	37

are utilized. DEC and sFEM can be applied to all surfaces, where a suitable surface mesh is available. DEC requires well-centered simplicial surface elements, whereas the requirements for sFEM are less restrictive. However, a non-regular shape of the triangles may increase the condition number of the resulting linear system (Olshanskii et al. 2013; Dziuk and Elliott 2013). Thus, the quality of the surface triangulation matters for both approaches. DI uses an implicit description of the surface and thus does not rely on an approximate surface mesh. The 3D domain Ω can be adaptively triangulated using regular shaped tetrahedra and thus allows to conserve good mesh quality easily. Efficient methods to calculate a signed-distance function $d_{\mathcal{S}}$ from an implicit description of $\mathcal{S}$ or from a triangulated surface are necessary and available for tetrahedral meshes, see Bornemann and Rasch (2006), Stöcker (2008).

The computational costs for all the methods vary a lot. Denoting by $|\mathcal{V}|$ the number of vertices of a surface triangulation and by $|\mathcal{E}|$ the number of edges. For SPH the main computational expenses are related to the forward and backward transform, which can be classified as $\mathcal{O}(N^2 \log N + |\mathcal{V}|)$ with bandwidth N, typically $N \sim \sqrt{|\mathcal{V}|}$. The other methods have to assemble and invert a linear system in each time step iteration. The number of degrees of freedom (DOFs) and the corresponding average number of nonzero entries (NNZ) per row in the linear system are summarized in Table 3. The total number of nonzeros in the system is approximately the same for DEC and sFEM, whereas DI produces a much larger and denser system.

The structure of the linear systems is also different. Where the sFEM and DI method produce symmetric matrices for symmetric differential operators, the DEC approach results in a non-symmetric matrix, since not all triangles in the discretization are equilateral. This restricts the choice of linear solvers and often results in an additional performance overhead.

DI allows to use classical finite element software. The additional cost, resulting from the treatment in 3D, can be reduced by adaptive refinement in a narrowband around the surface. This establishes this approach as an easy to use tool also in the context of surface vector field calculations. A further extension of the analyzed models toward evolving surfaces can also most easily be adopted to DI methods by evolving the implicit function or the phase-field variable.

6 Conclusion and Outlook

We presented a brief derivation of the weak surface Frank–Oseen energy as a thin-film limit of the well-known 3D Frank–Oseen distortion energy. By penalizing the unity of the vector field, the limit can be established for surfaces with $\chi(\mathcal{S}) \neq 0$. We highlight the importance of intrinsic and extrinsic energy contributions. Dynamic equations for

surface bound polar order are obtained by an L^2-gradient flow approach, leading to a vector-valued surface PDE.

The energy and the dynamic equations have been adapted to suit several numerical methods. The least approximating methods base on a direct discretization of the vector-valued state space of the energy functional. For spherical surfaces, this is SPH and for arbitrary surfaces DEC. Extending the variational space to arbitrary vector fields allowed us to split the vector-valued problem into a set of coupled scalar-valued problems for each component. Established solution procedures for such problems, as sFEM and DI, are adapted to this situation. Numerical experiments on the canonical unit sphere and surfaces with non-constant curvature established the consistency of all introduced methods.

The experiments further showed the tight interplay of topology, geometry, and dynamics. In all experiments, the defect localization is related to the Gaussian curvature of the surface, $+1$ defects are found at extrema of the Gaussian curvature, while -1 defects are located at saddle points. We have further demonstrated the general possibility to reduce the overall energy by introducing additional defects and thus establishing non-trivial realizations of the Poincaré–Hopf theorem as energy minima. The proposed methods allow to further investigate this interplay. Here the effect of ω_n as well as the impact of intrinsic and extrinsic contributions should be analyzed.

The introduced models and methods should also be complemented by more rigorous theoretical works on the convergence of the thin-film limit. In analogy to scalar-valued problems, an extension to evolving surfaces seems feasible. Beyond the mentioned fundamental issues, the model and methods are ready to be applied in the field of passive and active soft matter and surface bound, non-equilibrium physics comprising orientational order. Examples are passive (Vitelli and Nelson 2006; Lopez-Leon et al. 2011; Koning et al. 2013) and active (Menzel and Löwen 2013) liquid crystals and polar fluids (Ahmadi et al. 2006; Bois et al. 2011; Kruse et al. 2004) in thin shells, which are proposed models for a cell cortex (Ramaswamy and Jülicher 2016).

Although the polar model, described by the Frank–Oseen energy and the introduced dynamic equations, already shows a variety of interesting effects, a nematic model will have additional features. Therefore, the Q-tensor Landau–de Gennes models should be focused on. With similar ideas of incorporating a tangentiality penalization, a weak Q-tensor model on a surface could be derived and analyzed.

Acknowledgements This work is partially supported by the German Research Foundation through Grant Vo889/18. We further acknowledge computing resources provided at JSC under Grant HR06.

Appendix A: Thin-Film Limit of Penalized Frank–Oseen Energy

Considering a thin shell $\Omega_\delta = \mathcal{S} \times [-\delta/2, \delta/2]$ around the surface $\mathcal{S}$ with thickness δ, the local coordinates θ and φ of the surface immersion $\mathbf{x}$ and an additional coordinate ξ, which acts along the surface normal $\boldsymbol{\nu}$, lead to a thin shell parametrization $\widetilde{\mathbf{x}} : U_\delta \to \mathbb{R}^3$ for the parameter domain $U_\delta := U \times [-\delta/2, \delta/2]$, with $\widetilde{\mathbf{x}}$ defined by

$$\widetilde{\mathbf{x}}(\theta, \varphi, \xi) = \mathbf{x}(\theta, \varphi) + \xi \boldsymbol{\nu}(\theta, \varphi). \tag{81}$$

The thickness δ is sufficiently small to guarantee the injectivity of the pushforward, see Napoli and Vergori (2012b).

For a better readability, we denote indices which mark all three components $\{\theta, \varphi, \xi\}$ by capital letters. The indices for the surface components $\{\theta, \varphi\}$ are denoted by small letters. The metric tensor $\widetilde{\mathbf{g}}$ of the thin shell is given by its components $\widetilde{g}_{IJ} = \partial_I \widetilde{\mathbf{x}} \cdot \partial_J \widetilde{\mathbf{x}}$, i.e.,

$$\widetilde{g}_{ij} = g_{ij} - 2\xi \mathcal{B}_{ij} + \mathcal{O}(\xi^2)_{ij} = g_{ij} + \mathcal{O}(\xi)_{ij}, \quad \widetilde{g}_{\xi\xi} = 1 \text{ and } \widetilde{g}_{i\xi} = \widetilde{g}_{\xi i} = 0. \tag{82}$$

The pure formal indices on $\mathcal{O}$ extend the asymptotic polynomial behavior to tensor context and preserve summation conventions. Hence, for the Christoffel symbols $\widetilde{\Gamma}^K_{IJ} = \frac{1}{2}\widetilde{g}^{KL}\left(\partial_I \widetilde{g}_{JL} + \partial_J \widetilde{g}_{IL} - \partial_L \widetilde{g}_{IJ}\right)$, we obtain

$$\begin{aligned} &\widetilde{\Gamma}^k_{ij} = \Gamma^k_{ij} + \mathcal{O}(\xi)^k_{ij}, \quad \widetilde{\Gamma}^\xi_{ij} = \mathcal{B}_{ij} + \mathcal{O}(\xi)_{ij}, \quad \widetilde{\Gamma}^k_{i\xi} = \widetilde{\Gamma}^k_{\xi i} = -\mathcal{B}_i{}^k + \mathcal{O}(\xi)^k_i, \\ &\widetilde{\Gamma}^K_{\xi\xi} = \widetilde{\Gamma}^\xi_{I\xi} = \widetilde{\Gamma}^\xi_{\xi I} = 0. \end{aligned} \tag{83}$$

We can approximate the square root of the determinant $|\widetilde{\mathbf{g}}|$ on $\mathcal{S}$ by $\sqrt{|\widetilde{\mathbf{g}}|} = \sqrt{\widetilde{g}_{\xi\xi}|\mathbf{g}|} + \mathcal{O}(\xi) = (1 + \mathcal{O}(\xi))\sqrt{|\mathbf{g}|}$. Therefore, the volume element becomes

$$\mathrm{d}V = \sqrt{|\widetilde{\mathbf{g}}|}\, d\xi \wedge d\theta \wedge d\varphi = (1 + \mathcal{O}(\xi))\, d\xi \wedge \mathrm{d}\mathcal{S}. \tag{84}$$

The 3-tensor, with the same qualities as the volume element, is the Levi–Civita tensor

$$\widetilde{E}_{IJK} = \mathrm{d}V\left(\partial_I \widetilde{\mathbf{x}}, \partial_J \widetilde{\mathbf{x}}, \partial_K \widetilde{\mathbf{x}}\right) = \sqrt{|\widetilde{\mathbf{g}}|}\varepsilon_{IJK} = \sqrt{|\mathbf{g}|}\varepsilon_{IJK} + \mathcal{O}(\xi)_{IJK}, \tag{85}$$

with the common Levi–Civita symbols $\varepsilon_{IJK} \in \{-1, 0, 1\}$. With the Levi–Civita tensor $\mathbf{E}$ on the surface, defined by $E_{ij} = \mathrm{d}\mathcal{S}\left(\partial_i \mathbf{x}, \partial_j \mathbf{x}\right) = \sqrt{|\mathbf{g}|}\varepsilon_{ij}$, and the fact that all non-vanishing components of the Levi–Civita tensor $\widetilde{\mathbf{E}}$ in the thin shell have exactly one ξ-index, we obtain

$$\widetilde{E}_{\xi ij} = -\widetilde{E}_{i\xi j} = \widetilde{E}_{ij\xi} = E_{ij} + \mathcal{O}(\xi)_{ij}. \tag{86}$$

For a better distinction, we use a semicolon in the thin shell and a straight line on the surface to mark the components of the covariant derivative, i.e., for the vector fields $\widetilde{\mathbf{p}} \in C^1\left(\Omega_\delta, \mathsf{T}\Omega_\delta\right)$ and $\mathbf{p} \in C^1\left(\mathcal{S}, \mathsf{T}\mathcal{S}\right)$, we write

$$\widetilde{\mathrm{p}}^I_{;J} = \partial_J \widetilde{\mathrm{p}}^I + \widetilde{\Gamma}^I_{JK}\widetilde{\mathrm{p}}^K \text{ and} \tag{87}$$

$$p^i{}_{|j} = \partial_j p^i + \Gamma^i_{jk} p^k. \tag{88}$$

The contravariant derivatives are given by $\widetilde{\mathrm{p}}^{I;J} = \widetilde{g}^{JK}\widetilde{\mathrm{p}}^I_{;K}$ and $p^{i|j} = g^{jk} p^i{}_{|k}$. Henceforward, we assume that $\widetilde{\mathbf{p}} \in \mathsf{T}\Omega_\delta$ is an extension of $\mathbf{p}$, i.e., $\widetilde{\mathbf{p}}\big|_{\mathcal{S}} = \mathbf{p} \in \mathsf{T}\mathcal{S}$, and $\widetilde{\mathbf{p}}$ is parallel and length preserving in direction of $\boldsymbol{\nu}$, i.e., $\widetilde{\mathrm{p}}^I_{;\xi} = 0$ as a consequence.

Therefore, the Taylor approximation on the surface of the contravariant tangential components becomes

$$\begin{aligned}\widetilde{\mathrm{p}}^i &= p^i + \xi\,\partial_\xi \widetilde{\mathrm{p}}^i\big|_{\mathcal{S}} + \mathcal{O}(\xi^2)^i = p^i + \xi\left(\widetilde{\mathrm{p}}^i_{;\xi} - \widetilde{\Gamma}^i_{\xi K}\widetilde{\mathrm{p}}^K\big|_{\mathcal{S}}\right) + \mathcal{O}(\xi^2)^i \\ &= p^i + \xi\,\mathcal{B}_k{}^i\, p^k + \mathcal{O}(\xi^2)^i.\end{aligned} \tag{89}$$

It holds $\widetilde{\mathrm{p}}^\xi = 0$, because $\widetilde{\mathrm{p}}^\xi\big|_{\mathcal{S}} = 0$ and $\partial_\xi \widetilde{\mathrm{p}}^\xi = \widetilde{\mathrm{p}}^\xi_{;\xi} - \widetilde{\Gamma}^\xi_{\xi K}\widetilde{\mathrm{p}}^K = 0$, but nonetheless, we get non-vanishing covariant tangential derivatives

$$\widetilde{\mathrm{p}}^\xi_{;j} = \widetilde{\Gamma}^\xi_{jK}\widetilde{\mathrm{p}}^K = \mathcal{B}_{jk}p^k + \mathcal{O}(\xi)_j. \tag{90}$$

All remaining covariant derivatives can be approximated by

$$\widetilde{\mathrm{p}}^i_{;j} = \partial_j \widetilde{\mathrm{p}}^i + \widetilde{\Gamma}^i_{jK}\widetilde{\mathrm{p}}^K = \partial_j \mathrm{p}^i + \Gamma^i_{jk}\mathrm{p}^k + \mathcal{O}(\xi)^i_j = p^i{}_{|j} + \mathcal{O}(\xi)^i_j. \tag{91}$$

The divergence of a vector field is the trace of its covariant derivative reads

$$\nabla\cdot\widetilde{\mathbf{p}} = \widetilde{\mathrm{p}}^I_{;I} = \widetilde{\mathrm{p}}^i_{;i} = p^i{}_{|i} + \mathcal{O}(\xi) = \operatorname{div}\mathbf{p} + \mathcal{O}(\xi). \tag{92}$$

The covariant curl of a vector field can be obtained by a double contraction of the Levi–Civita tensor and the contravariant derivative, i.e.,

$$\left[\nabla\times\widetilde{\mathbf{p}}\right]_I = -\widetilde{E}_{IJK}\widetilde{\mathrm{p}}^{J;K}. \tag{93}$$

With (86), the ξ-component of the curl can be approximated by

$$\left[\nabla\times\widetilde{\mathbf{p}}\right]_\xi = -E_{jk}\widetilde{g}^{kL}\widetilde{\mathrm{p}}^j_{;L} + \mathcal{O}(\xi) = -E_{jk}g^{kl}p^j{}_{|l} + \mathcal{O}(\xi) = \operatorname{rot}\mathbf{p} + \mathcal{O}(\xi) \tag{94}$$

and the covariant tangential components by

$$\begin{aligned}\left[\nabla\times\widetilde{\mathbf{p}}\right]_i &= -\left(\widetilde{E}_{ij\xi}\widetilde{\mathrm{p}}^{j;\xi} + \widetilde{E}_{i\xi j}\widetilde{\mathrm{p}}^{\xi;j}\right) = E_{ij}\widetilde{g}^{jK}\widetilde{\mathrm{p}}^\xi_{;K} + \mathcal{O}(\xi)_i \\ &= E_{ij}\mathcal{B}^j{}_l\,p^l + \mathcal{O}(\xi)_i = -[*(\mathcal{B}\mathbf{p})^\flat]_i + \mathcal{O}(\xi)_i,\end{aligned} \tag{95}$$

where we use, that for a every $\mathbf{q}\in\mathsf{T}\mathcal{S}$

$$*\mathbf{q}^\flat = \mathbf{i}_\mathbf{q}(\,\mathrm{d}\mathcal{S}) = \sqrt{|\mathbf{g}|}\left(-q^\theta d\varphi + q^\varphi d\theta\right) = -\mathbf{E}\mathbf{q} \tag{96}$$

is valid on $\mathcal{S}$, see Abraham et al. (1988). The Hodge star operator is length preserving and the metric $\widetilde{\mathbf{g}}$ induces the common norm in the thin shell; therefore, it holds

$$\|\nabla\times\widetilde{\mathbf{p}}\|^2_{\Omega_\delta} = \left\|-*\,(\mathcal{B}\mathbf{p})^\flat\right\|^2_{\mathcal{S}} + \widetilde{g}^{\xi\xi}\,(\operatorname{rot}\mathbf{p})^2 + \mathcal{O}(\xi) = \|\mathcal{B}\mathbf{p}\|^2_{\mathcal{S}} + (\operatorname{rot}\mathbf{p})^2 + \mathcal{O}(\xi).$$

Finally, with $\|\widetilde{\mathbf{p}}\|^2_{\Omega_\delta} = \|\mathbf{p}\|^2_{\mathcal{S}} + \mathcal{O}(\xi)$, (84), (92), (94), and (95), we can approximate the penalized Frank–Oseen energy (3) in the thin shell Ω_δ by

$$\begin{aligned} F_{\omega_\mathrm{n}}\left[\widetilde{\mathbf{p}}, \Omega_\delta\right] &= \int_{\mathcal{S}} \int_{-\delta/2}^{\delta/2} \frac{K}{2} \Big((\operatorname{div} \mathbf{p})^2 + (\operatorname{rot} \mathbf{p})^2 \\ &\qquad + \|\mathcal{B}\mathbf{p}\|^2_{\mathcal{S}} \Big) + \frac{\omega_\mathrm{n}}{4} \Big(\|\mathbf{p}\|^2_{\mathcal{S}} - 1 \Big)^2 + \mathcal{O}(\xi)\, d\xi \wedge \mathrm{d}\mathcal{S} \\ &= \delta \left(F^{\mathcal{S}}_{\omega_\mathrm{n}}[\mathbf{p}] + \mathcal{O}(\delta) \right) \end{aligned}$$

for $\widetilde{\mathbf{p}} \in H^{\mathrm{DR}}(\Omega_\delta;\, \mathsf{T}\Omega_\delta)$ and $\mathbf{p} \in H^{\mathrm{DR}}(\mathcal{S};\, \mathsf{T}\mathcal{S})$.

Appendix B: Integral Theorems

The exterior derivative $\mathbf{d}$ is the L^2-adjoint of $(- * \mathbf{d} *)$. This allows to obtain some frequently used integral identities for the tangential vector field $\mathbf{p} = \boldsymbol{\alpha}^\sharp : \mathcal{S} \to \mathsf{T}\mathcal{S}$ on a closed surface $\mathcal{S}$ and also for its $\mathbb{R}^3$ extension $\widehat{\mathbf{p}} : \mathcal{S} \to \mathbb{R}^3$, with $\mathbf{p} = \pi_{\mathsf{T}\mathcal{S}} \widehat{\mathbf{p}}$. We get

$$\begin{aligned} -\int_{\mathcal{S}} \langle \operatorname{grad} f, \widehat{\mathbf{p}} \rangle \, \mathrm{d}\mathcal{S} &= -\int_{\mathcal{S}} \langle \operatorname{grad} f, \mathbf{p} \rangle \, \mathrm{d}\mathcal{S} = -\int_{\mathcal{S}} \langle \mathbf{d} f, \boldsymbol{\alpha} \rangle \, \mathrm{d}\mathcal{S} \\ &= \int_{\mathcal{S}} f * \mathbf{d} * \boldsymbol{\alpha} \, \mathrm{d}\mathcal{S} = \int_{\mathcal{S}} f \operatorname{div} \mathbf{p} \, \mathrm{d}\mathcal{S} \\ &= \int_{\mathcal{S}} f \operatorname{div}(\pi_{\mathsf{T}\mathcal{S}} \widehat{\mathbf{p}}) \, \mathrm{d}\mathcal{S} = \int_{\mathcal{S}} f \operatorname{div} \widehat{\mathbf{p}} - \mathcal{H}\, (\widehat{\mathbf{p}} \cdot \boldsymbol{\nu}) \, \mathrm{d}\mathcal{S} \end{aligned}$$

and

$$\begin{aligned} -\int_{\mathcal{S}} \langle \operatorname{rot} f, \widehat{\mathbf{p}} \rangle \, \mathrm{d}\mathcal{S} &= -\int_{\mathcal{S}} \langle \operatorname{rot} f, \mathbf{p} \rangle \, \mathrm{d}\mathcal{S} = -\int_{\mathcal{S}} \langle * \mathbf{d} f, \boldsymbol{\alpha} \rangle \, \mathrm{d}\mathcal{S} \\ &= \int_{\mathcal{S}} \langle \mathbf{d} f, * \boldsymbol{\alpha} \rangle \, \mathrm{d}\mathcal{S} = -\int_{\mathcal{S}} f * \mathbf{d} * * \boldsymbol{\alpha} \, \mathrm{d}\mathcal{S} = \int_{\mathcal{S}} f \operatorname{rot} \mathbf{p} \, \mathrm{d}\mathcal{S} \\ &= \int_{\mathcal{S}} f \operatorname{rot}(\pi_{\mathsf{T}\mathcal{S}} \widehat{\mathbf{p}}) \, \mathrm{d}\mathcal{S} = \int_{\mathcal{S}} f \operatorname{rot} \widehat{\mathbf{p}} \, \mathrm{d}\mathcal{S}. \end{aligned}$$

Note that $** \alpha = -\alpha$ and the inner product is invariant with respect to $*$, $\flat$, and $\sharp$, applied to both arguments of the product simultaneously, see Abraham et al. (1988). Hence, we obtain for the Laplace–deRham operator

$$\begin{aligned} \int_{\mathcal{S}} \left\langle \boldsymbol{\Delta}^{\mathrm{dR}} \mathbf{p}, \widehat{\mathbf{q}} \right\rangle \mathrm{d}\mathcal{S} &= \int_{\mathcal{S}} \left\langle \boldsymbol{\Delta}^{\mathrm{dR}} \mathbf{p}, \mathbf{q} \right\rangle \mathrm{d}\mathcal{S} = -\int_{\mathcal{S}} \langle \operatorname{grad} \operatorname{div} \mathbf{p}, \mathbf{q} \rangle + \langle \operatorname{rot} \operatorname{rot} \mathbf{p}, \mathbf{q} \rangle \, \mathrm{d}\mathcal{S} \\ &= \int_{\mathcal{S}} (\operatorname{div} \mathbf{p})(\operatorname{div} \mathbf{q}) + (\operatorname{rot} \mathbf{p})(\operatorname{rot} \mathbf{q}) \, \mathrm{d}\mathcal{S} \\ &= \int_{\mathcal{S}} \operatorname{div}(\pi_{\mathsf{T}\mathcal{S}} \widehat{\mathbf{p}}) \operatorname{div}(\pi_{\mathsf{T}\mathcal{S}} \widehat{\mathbf{q}}) + \operatorname{rot}(\pi_{\mathsf{T}\mathcal{S}} \widehat{\mathbf{p}}) \operatorname{rot}(\pi_{\mathsf{T}\mathcal{S}} \widehat{\mathbf{q}}) \\ &= \int_{\mathcal{S}} (\operatorname{div} \widehat{\mathbf{p}} - \mathcal{H}\, (\widehat{\mathbf{p}} \cdot \boldsymbol{\nu}))(\operatorname{div} \widehat{\mathbf{q}} - \mathcal{H}\, (\widehat{\mathbf{q}} \cdot \boldsymbol{\nu})) + (\operatorname{rot} \widehat{\mathbf{p}})(\operatorname{rot} \widehat{\mathbf{q}}). \end{aligned}$$

Appendix C: Convergence Study of the Laplace–deRham Approximation

To justify the approximation $\boldsymbol{\Delta}^{\mathrm{dR}}\mathbf{p} \approx \widehat{\boldsymbol{\Delta}}^{\mathrm{dR}}\widehat{\mathbf{p}} + \omega_{\mathrm{t}}\boldsymbol{\nu}\,(\boldsymbol{\nu}\cdot\widehat{\mathbf{p}})$, we set up a test case consisting of a vector-valued Helmholtz equation on an ellipsoidal surface $\mathcal{S}^E$ (major axis: 1.0, 0.5, and 1.5)

$$-\boldsymbol{\Delta}^{\mathrm{dR}}\mathbf{p} + \mathbf{p} = -\boldsymbol{\Delta}^{\mathrm{dR}}\mathbf{p}_s + \mathbf{p}_s =: \mathbf{f} \quad \text{on } \mathcal{S}^E \tag{97}$$

with given analytical solution $\mathbf{p}_s = [-2y, 0.5x, 0]^{\mathrm{T}} \in C(\mathcal{S}^E, \mathsf{T}\mathcal{S}^E)$. We solve

$$-\widehat{\boldsymbol{\Delta}}^{\mathrm{dR}}\widehat{\mathbf{p}} + \widehat{\mathbf{p}} + \omega_{\mathrm{t}}\boldsymbol{\nu}\,(\boldsymbol{\nu}\cdot\widehat{\mathbf{p}}) = \mathbf{f} \quad \text{on } \mathcal{S}^E \tag{98}$$

using sFEM on a conforming triangulation $\mathcal{S}_h^E$ of $\mathcal{S}^E$ with piecewise linear Lagrange elements $\mathbb{V}_h(\mathcal{S}_h^E) = \{v_h \in C^0(\mathcal{S}_h^E) \;:\; v_h|_T \in \mathbb{P}^1,\ \forall\, T \in \mathcal{T}\}$ as trial and test space for all components $\hat{\mathrm{p}}_i$. This leads to a sequence of linear discrete equations

$$\begin{aligned}&\textstyle\int_{\mathcal{S}_h^E} \nabla_{\mathcal{S}}\cdot\widehat{\mathbf{p}} D_i\psi + \nabla_{\mathcal{S}}\cdot(\widehat{\mathbf{p}}\times\boldsymbol{\nu})\,\nabla_{\mathcal{S}}\cdot(\mathbf{e}_i\psi\times\boldsymbol{\nu})\;\mathrm{d}\mathcal{S}\\ &+\textstyle\int_{\mathcal{S}_h^E}\hat{\mathrm{p}}_i\psi\,\mathrm{d}\mathcal{S} + \omega_{\mathrm{t}}\int_{\mathcal{S}_h^E} v_i\,(\boldsymbol{\nu}\cdot\widehat{\mathbf{p}})\,\psi\,\mathrm{d}\mathcal{S} = \textstyle\int_{\mathcal{S}_h^E} f_i\psi\,\mathrm{d}\mathcal{S}.\end{aligned} \tag{99}$$

To assemble and solve the resulting system, we use the FEM toolbox AMDiS (Vey and Voigt 2007; Witkowski et al. 2015).

Figure 9 shows the L^2-error $\epsilon_{L^2}(\mathbf{p}) = \left(\int_{\mathcal{S}^E}\sum_{i=1}(\widehat{\mathbf{p}}_i - \mathrm{p}_{s,i})^2\,\mathrm{d}\mathcal{S}\right)^{1/2}$ vs ω_{t} and linear convergence, which is only limited by the mesh quality.

As a complementary result and to emphasize the delicate nature of the coupling between curvature and spatial derivatives, we also show in Fig. 9 the L^2-error of a componentwise approximation of $\boldsymbol{\Delta}^{\mathrm{dR}}$

$$\boldsymbol{\Delta}^{\mathrm{dR}}\mathbf{p} \approx \sum_{i=i}^{3}\nabla_{\mathcal{S}}\cdot\nabla_{\mathcal{S}}\hat{\mathrm{p}}_i\mathbf{e}_i + \omega_{\mathrm{t}}\boldsymbol{\nu}\,(\boldsymbol{\nu}\cdot\widehat{\mathbf{p}})\,. \tag{100}$$

As clearly visible in Fig. 9, this approximation fails for any values of ω_{t} to reproduce the $\boldsymbol{\Delta}^{\mathrm{dR}}$ behavior on $\mathcal{S}^E$.

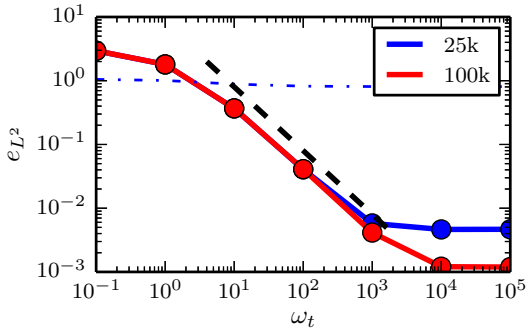

Fig. 9 L^2-error for $\widehat{\boldsymbol{\Delta}}^{\mathrm{dR}}$ approximation (*solid lines*) for two well-centered triangulations of $\mathcal{S}^E$ with $25k$ and $100k$ vertices. The *black dashed line* indicates linear rate of convergence. The *dash doted line* shows the result for a componentwise approximation of $\boldsymbol{\Delta}^{\mathrm{dR}}$ in (100) (Color figure online)

Appendix D: DEC—Notations and Details

D.1: Notations

We often use the strict order relation $\succ$ and $\prec$ on simplices, where $\succ$ is proverbial the "contains" relation, i.e., $e \succ v$ means: the edge e contains the vertex v. Correspondingly is $\prec$ the "part of" relation, i.e., $v \prec T$ means: the vertex v is part of the face T. Hence, we can use this notation also for sums, like $\sum_{T \succ e}$, i.e., the sum over all faces T containing edge e, or $\sum_{v \prec e}$, i.e., the sum over all vertices v being part of edge e. Sometimes we need to determine this relation for edges more precisely with respect to the orientation. Therefore, a sign function is introduced,

$$s_{T,e} := \begin{cases} +1 & \text{if } e \prec T \text{ and } T \text{ is on left side of } e \\ -1 & \text{if } e \prec T \text{ and } T \text{ is on right side of } e \\ 0 & e \not\prec f, \end{cases} \tag{101}$$

$$s_{v,e} := \begin{cases} +1 & \text{if } v \prec e \text{ and } e \text{ points to } v \\ -1 & \text{if } v \prec e \text{ and } e \text{ points away from } v \\ 0 & v \not\prec e, \end{cases} \tag{102}$$

to describe such relations between faces and edges, or vertices and edges, respectively. Figure 10 gives a schematic picture.

The property of primal mesh to be well centered ensures the existence of a Voronoi mesh (dual mesh), which is also an orientable manifold-like simplicial complex, but not well centered.

The basis of the Voronoi mesh is not simplices, but chains of them. To identify these basic chains, we apply the (geometrical) star operator $\star$ on the primal simplices,

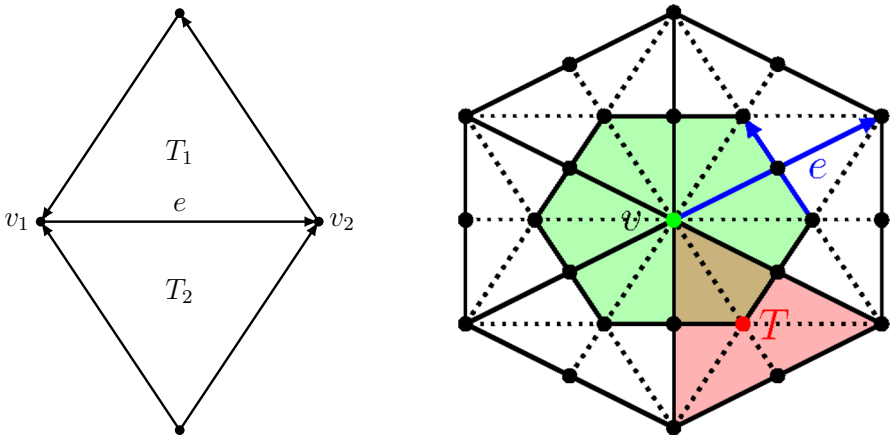

Fig. 10 *Left* this simple example mesh leads to $s_{T_1,e} = +1$, $s_{T_2,e} = -1$, $s_{v_1,e} = -1$ and $s_{v_2,e} = +1$. *Right* the vertex v (*green*) and its Voronoi cell $\star v$ (*semitransparent green*); the edge e (*blue*) and its Voronoi edge $\star e$ (*blue*); the face T (*semitransparent red*) and its Voronoi vertex (*red*) (Color figure online)

i.e., $\star v$ is the Voronoi cell corresponding to the vertex v and inherits its orientation from the orientation of the polytope $|\mathcal{K}|$. $\star v$ is, from a geometric point of view, the convex hull of circumcenters $c(T)$ of all triangles $T \succ v$. The Voronoi edge $\star e$ of an edge e is a connection of the right face $T_2 \succ e$ with the left face $T_1 \succ e$ over the midpoint $c(e)$. The Voronoi vertex $\star T$ of a face T is simply its circumcenter $c(T)$ (see Fig. 10). For greater details and a more mathematical discussion, see, e.g., Hirani (2003), VanderZee et al. (2010).

The boundary operator ∂ maps simplices (or chains of them) to the chain of simplices that describes its boundary, with respect to its orientation (see Hirani 2003), e.g., $\partial(\star v) = -\sum_{e \succ v} s_{v,e}(\star e)$ (formal sum for chains) and $\partial e = \sum_{v \prec e} s_{v,e} v$.

The expression $|\cdot|$ measures the volume of a simplex, i.e., $|T|$ the area of the face T, $|e|$ the length of the edge e, and the zero-dimensional volume $|v|$ are set to be 1. Therefore, the volume is also defined for chains and the dual mesh, since the integral is a linear functional.

D.2: Laplace Operators

With the Stokes theorem and the discrete Hodge operator defined in Hirani (2003), we can develop a DEC discretized Rot-Rot-Laplace for a discrete 1-form $\alpha \in \Lambda_h^1(\mathcal{K})$ by

$$\begin{aligned}
\boldsymbol{\Delta}_h^{\mathrm{RR}}\alpha(e) &:= (*\mathbf{d} * \mathbf{d}\alpha)(e) = -\frac{|e|}{|\star e|}(\mathbf{d} * \mathbf{d}\alpha)(\star e) \\
&= -\frac{|e|}{|\star e|}(*\mathbf{d}\alpha)(\partial \star e) = -\frac{|e|}{|\star e|}\sum_{T \succ e} s_{T,e}(*\mathbf{d}\alpha)(\star T) \\
&= -\frac{|e|}{|\star e|}\sum_{T \succ e}\frac{s_{T,e}}{|T|}(\mathbf{d}\alpha)(T) = -\frac{|e|}{|\star e|}\sum_{T \succ e}\frac{s_{T,e}}{|T|}\alpha(\partial T) \\
&= -\frac{|e|}{|\star e|}\sum_{T \succ e}\frac{s_{T,e}}{|T|}\sum_{\tilde{e} \prec T} s_{T,\tilde{e}}\alpha(\tilde{e})
\end{aligned} \tag{103}$$

and a DEC discretized Grad-Div-Laplace by

$$\begin{aligned}
\boldsymbol{\Delta}_h^{\mathrm{GD}}\alpha(e) &:= (\mathbf{d} * \mathbf{d} * \alpha)(e) = (*\mathbf{d} * \alpha)(\partial e) \\
&= \sum_{v \prec e} s_{v,e}(*\mathbf{d} * \alpha)(v) = \sum_{v \prec e}\frac{s_{v,e}}{|\star v|}(\mathbf{d} * \alpha)(\star v) \\
&= \sum_{v \prec e}\frac{s_{v,e}}{|\star v|}(*\alpha)(\partial \star v) = -\sum_{v \prec e}\frac{s_{v,e}}{|\star v|}\sum_{\tilde{e} \succ v} s_{v,\tilde{e}}(*\alpha)(\star \tilde{e}) \\
&= -\sum_{v \prec e}\frac{s_{v,e}}{|\star v|}\sum_{\tilde{e} \succ v} s_{v,\tilde{e}}\frac{|\star \tilde{e}|}{|\tilde{e}|}\alpha(\tilde{e}).
\end{aligned} \tag{104}$$

Hence, we obtain the DEC discretized Laplace–deRham operator by

$$\boldsymbol{\Delta}_h^{\mathrm{dR}}\alpha(e) = -\boldsymbol{\Delta}_h^{\mathrm{RR}}\alpha(e) - \boldsymbol{\Delta}_h^{\mathrm{GD}}\alpha(e).$$

D.3: Conflate Linear Operators and Its Hodge Dual to a PD-(1, 1)-Tensor

For a linear operator $\mathbf{M} : \mathsf{T}^*\mathcal{S} \to \mathsf{T}^*\mathcal{S}$ pointwise defined as a mixed co- and contravariant (1,1)-tensor with components $M_i{}^j$, we discretize the 1-form $\mathbf{M}\boldsymbol{\alpha}$ on an edge $e \in \mathcal{E}$ by definition (27) and approximate the operator on the projected midpoint of the edge, i.e.,

$$(\mathbf{M}\boldsymbol{\alpha})_h(e) = \int_{\pi(e)} M_i{}^j \alpha_j \, \mathrm{d}x^i \approx [\mathbf{M}(e)]_{ik}\, g^{kj} \int_{\pi(e)} \alpha_j \mathrm{d}x^i, \tag{105}$$

with $\mathbf{M}(e) := \mathbf{M}|_{\pi(c(e))}$. With respect to an orthogonal basis $\{\partial_i \mathbf{x}, \partial_j \mathbf{x}\}$ with metric tensor $\mathbf{g} = g_i (dx^i)^2$, we obtain for the 1-form $\boldsymbol{\alpha} = \alpha_i dx^i$ the Hodge dual

$$*\boldsymbol{\alpha} = [*\alpha]_1 dx^1 + [*\alpha]_2 dx^2 = -\sqrt{\frac{g_1}{g_2}}\alpha_2 dx^1 + \sqrt{\frac{g_2}{g_1}}\alpha_1 dx^2. \tag{106}$$

Hence, we can replace the 1-forms beneath the integrals by

$$\begin{bmatrix} \alpha_1 dx^1 & \alpha_2 dx^1 \\ \alpha_1 dx^2 & \alpha_2 dx^2 \end{bmatrix} = \begin{bmatrix} \alpha_1 dx^1 & -\sqrt{\frac{g_2}{g_1}}[*\alpha]_1 dx^1 \\ \sqrt{\frac{g_1}{g_2}}[*\alpha]_2 dx^2 & \alpha_2 dx^2 \end{bmatrix}. \tag{107}$$

Now, we use the basis $\{\mathbf{e}, \mathbf{e}_\star\}$ defined in Sect. 4.2 on the polytope $|\mathcal{K}|$ and the resulting metric (34), i.e., $g_1 = |e|^2$ and $g_2 = |\star e|^2$. This leads to an approximation of $(\mathbf{M}\boldsymbol{\alpha})_h \in \Lambda^1_h(\mathcal{K})$ as a linear combination of $\alpha_h, (*\alpha)_h \in \Lambda^1_h(\mathcal{K})$, or rather, evaluated on an edge $e \in \mathcal{E}$

$$(\mathbf{M}\boldsymbol{\alpha})_h(e) \approx \frac{1}{|e|^2} M_{\mathbf{e},\mathbf{e}}(e)\alpha_h(e) - \frac{1}{|e||\star e|} M_{\mathbf{e},\mathbf{e}_\star}(*\alpha)_h(e) \tag{108}$$

and, in general, for $\mathbf{v}, \mathbf{w} \in \mathrm{Span}\{\mathbf{e}, \mathbf{e}_\star\}$ is $M_{\mathbf{v},\mathbf{w}}(e) = \mathbf{v} \cdot \mathbf{M}(e) \cdot \mathbf{w} = v^i\, [\mathbf{M}(e)]_{ij}\, w^j$ the evaluation of the complete covariant tensor $\mathbf{M}(e)$ in direction $\mathbf{v}$ and $\mathbf{w}$. Note, if $\mathbf{M} \in \mathsf{T}\mathcal{S} \times \mathsf{T}\mathcal{S}$ is formulated in Euclidean $\mathbb{R}^3$ coordinates, so that $\mathbf{M}(e) \in \mathbb{R}^{3\times 3}$, there is no distinction between co- and contravariant components of $\mathbf{M}(e)$. Furthermore, if we use the approximation $(*\mathbf{M}\boldsymbol{\alpha})_h(e) \approx -\frac{|e|}{|\star e|}(\mathbf{M}\boldsymbol{\alpha})_h(\star e)$, we get with respect to (105) and (107)

$$(*\mathbf{M}\boldsymbol{\alpha})_h(e) \approx -\frac{1}{|e||\star e|} M_{\mathbf{e}_\star,\mathbf{e}}\alpha_h(e) + \frac{1}{|\star e|^2} M_{\mathbf{e}_\star,\mathbf{e}_\star}(*\alpha)_h(e). \tag{109}$$

Finally, we can summarize (108) and (109) with the PD-1-form $\underline{\boldsymbol{\alpha}} \in \Lambda^1_h(\mathcal{K}; \mathfrak{T}^*\mathcal{E})$ on every edge $e \in \mathcal{E}$ to

$$\underline{\underline{\mathbf{M}}} \cdot \underline{\boldsymbol{\alpha}} := \begin{bmatrix} \frac{1}{|e|^2} M_{\mathbf{e},\mathbf{e}} & -\frac{1}{|e||\star e|} M_{\mathbf{e},\mathbf{e}_\star} \\ -\frac{1}{|e||\star e|} M_{\mathbf{e}_\star,\mathbf{e}} & \frac{1}{|\star e|^2} M_{\mathbf{e}_\star,\mathbf{e}_\star} \end{bmatrix} \cdot \underline{\boldsymbol{\alpha}} \approx \begin{bmatrix} (\mathbf{M}\boldsymbol{\alpha})_h \\ (*\mathbf{M}\boldsymbol{\alpha})_h \end{bmatrix}, \tag{110}$$

where the evaluation argument e is omitted for a better readability.

References

Abraham, R., Marsden, J.E., Ratiu, T.S.: Manifolds, Tensor Analysis, and Applications, No. Bd. 75 in Applied Mathematical Sciences. Springer, New York (1988)

Ahmadi, A., Marchetti, M.C., Liverpool, T.B.: Hydrodynamics of isotropic and liquid crystalline active polymer solutions. Phys. Rev. E **74**, 061913 (2006)

Aland, A., Boden, S., Hahn, A., Klingbeil, F., Weismann, M., Weller, S.: Quantitative comparison of Taylor flow simulations based on sharp- and diffuse-interface models. Int. J. Numer. Methods Fluids **73**, 344–361 (2013)

Aland, S., Lowengrub, J., Voigt, A.: Two-phase flow in complex geometries: a diffuse domain approach. Comput. Model. Eng. Sci. **57**, 77–108 (2010)

Aland, S., Lowengrub, J., Voigt, A.: A continuum model for colloid-stabilized interfaces. Phys. Fluids **23**, 062103 (2011)

Aland, S., Rätz, A., Röger, M., Voigt, A.: Buckling instability of viral capsides—a continuum approach. Multiscale Model Simul. **10**, 82–110 (2012)

Arnold, D.N., Falk, R.S., Winther, R.: Finite element exterior calculus, homological techniques, and applications. Acta Numer. **15**, 1–155 (2006)

Arnold, D.N., Falk, R.S., Winther, R.: Finite element exterior calculus: from Hodge theory to numerical stability. Bull. Am. Math. Soc. **47**, 281–354 (2010)

Backofen, R., Gräf, M., Potts, D., Praetorius, S., Voigt, A., Witkowski, T.: A continuous approach to discrete ordering on $\mathbb{S}^2$. Multiscale Model. Simul. **9**, 314–334 (2011)

Backus, G.E.: Potentials for tangent tensor fields on spheroids. Arch. Ration. Mech. Anal. **22**, 210–252 (1966)

Ball, J.M.: Mathematics and liquid crystals. Mol. Cryst. Liq. Cryst. **647**, 1–27 (2017). doi:10.1080/15421406.2017.1289425

Ball, J.M., Zarnescu, D.A.: Orientability and energy minimization in liquid crystal models. Arch. Ration. Mech. Anal. **202**, 493–535 (2011)

Barrera, R.G., Estevez, G.A., Giraldo, J.: Vector spherical harmonics and their application to magnetostatics. Eur. J. Phys. **6**, 287 (1985)

Bertalmio, M., Cheng, L.T., Osher, S., Sapiro, G.: Variational problems and partial differential equations on implicit surfaces. J. Comput. Phys. **174**, 759–780 (2001)

Blumberg Selinger, R.L., Konya, A., Travesset, A., Selinger, J.V.: Monte Carlo studies of the XY model on two-dimensional curved surfaces. J. Phys. Chem. B **115**, 13989–13993 (2011)

Bois, J.S., Jülicher, F., Grill, S.W.: Pattern formation in active fluids. Phys. Rev. Lett. **106**, 028103 (2011)

Bornemann, F., Rasch, C.: Finite-element discretization of static Hamilton-Jacobi equations based on a local variational principle. Comput. Vis. Sci. **9**, 57–69 (2006)

Boyd, J.: Chebyshev and Fourier Spectral Methods, Dover Books on Mathematics, Second Revised edn. Dover Publications, New York (2001)

Burger, M., Stöcker, C., Voigt, A.: Finite element-based level set methods for higher order flows. J. Sci. Comput. **35**, 77–98 (2008)

Calhoum, D., Helzel, C., LeVeque, R.: Logically rectangular grids and finite volume methods for PDEs in circular and spherical domains. SIAM Rev. **50**, 723–752 (2008)

Chen, Y.: The weak solutions to the evolution problems of harmonic maps. Math. Zeitschr. **201**, 69–74 (1989)

Desbrun, M., Hirani, A.N., Leok, M., Marsden, J.E.: Discrete Exterior Calculus, arXiv Preprint, arXiv:math/0508341 (2005)

Duduchava, L.R., Mitrea, D., Mitrea, M.: Differential operators and boundary value problems on hypersurfaces. Math. Nachr. **279**, 996–1023 (2006)

Dziuk, G.: Finite elements for the Beltrami operator on arbitrary surfaces. In: Hildebrandt, S., Leis, R. (eds.) Partial differential equations and calulus of variations. Lecture Notes in Mathematics, vol. 1357, p. 142. Springer, Berlin (1988)

Dziuk, G., Elliott, C.M.: Finite elements on evolving surfaces. IMA J. Numer. Anal. **27**, 261 (2007)

Dziuk, G., Elliott, C.M.: Surface finite elements for parabolic equations. J. Comput. Math. **25**, 385 (2007)

Dziuk, G., Elliott, C.M.: Eulerian finite element method for parabolic PDEs on implicit surfaces. Interface Free Bound. **10**, 119 (2008)
Dziuk, G., Elliott, C.M.: Finite element methods for surface PDEs. Acta Numer. **22**, 289–396 (2013)
Eilks, C., Elliott, C.M.: Numerical simulation of dealloying by surface dissolution via the evolving surface finite element method. J. Chem. Phys. **227**, 9727–9741 (2008)
Fengler, M., Freeden, W.: A nonlinear Galerkin scheme involving vector and tensor spherical harmonics for solving the incompressible Navier–Stokes equation on the sphere. SIAM J. Sci. Comput. **27**, 967–994 (2005)
Frank, F.C.: I. Liquid crystals. On the theory of liquid crystals. Discuss. Faraday Soc. **25**, 19–28 (1958)
Freeden, W., Gervens, T., Schreiner, M.: Tensor spherical harmonics and tensor spherical splines. Manuscr. Geod. **19**, 80–100 (1994)
Freeden, W., Schreiner, M.: Spherical Functions of Mathematical Geosciences—A Scalar, Vectorial, and Tensorial Setup. Advances in Geophysical and Environmental Mechanics and Mathematics. Springer, Berlin (2009)
Freund, R.W.: A transpose-free quasi-minimal residual algorithm for non-Hermitian linear systems. SIAM J. Sci. Comput. **14**, 470–482 (1993)
Greer, J., Bertozzi, A.L., Sapiro, G.: Fourth order partial differential equations on general geometries. J. Chem. Phys. **216**, 216 (2006)
Hesthaven, J.S., Gottlieb, S., Gottlieb, D.: Spectral Methods for Time-Dependent Problems. Cambridge Monographs on Applied and Computational Mathematics, vol. 21. Cambridge University Press, Cambridge (2007)
Hirani, A.N.: Discrete Exterior Calculus. Ph.D. thesis, California Institute of Technology, Pasadena, CA, USA (2003)
Iyer, G., Xu, X., Zarnescu, D.A.: Dynamic cubic instability in a 2D Q-tensor model for liquid crystals. Math. Model. Methods Appl. Sci. **25**, 1477–1517 (2015)
Koning, V., Lopez-Leon, T., Fernandez-Nieves, A., Vitelli, V.: Bivalent defect configurations in inhomogeneous nematic shells. Soft Matter **9**, 4993–5003 (2013)
Kostelec, P.J., Maslen, D.K., Healy, D.M.J., Rockmore, D.N.: Computational harmonic analysis for tensor fields on the two-sphere. J. Comput. Phys. **162**, 514–535 (2000)
Kralj, S., Rosso, R., Virga, E.G.: Curvature control of valence on nematic shells. Soft Matter **7**, 670–683 (2011)
Kruse, K., Joanny, J.F., Jülicher, F., Prost, J., Sekimoto, K.: Asters, vortices, and rotating spirals in active gels of polar filaments. Phys. Rev. Lett. **92**, 078101 (2004)
Kunis, S., Potts, D.: Fast spherical Fourier algorithms. J. Comput. Appl. Math. **161**, 75–98 (2003)
Li, X., Lowengrub, J., Voigt, A., Rätz, A.: Solving PDEś in complex geometries: a diffuse domain approach. Commun. Math. Sci. **7**, 81–107 (2009)
Li, Y., Miao, H., Ma, H., Chen, J.Z.: Defect-free states and disclinations in toroidal nematics. RSC Adv. **4**, 27471–27480 (2014)
Lopez-Leon, T., Fernandez-Nieves, A., Nobili, M., Blanc, C.: Nematic-smectic transition in spherical shells. Phys. Rev. Lett. **106**, 247802 (2011)
Lopez-Leon, T., Koning, V., Devaiah, K.B.S., Vitelli, V., Fernandez-Nieves, A.: Frustrated nematic order in spherical geometries. Nat. Phys. **7**, 391–394 (2011)
Lowengrub, J., Rätz, A., Voigt, A.: Phase-field approximation of the dynamics of multicomponent vesicles: spinodal decomposition, coarsening, budding, and fission. Phys. Rev. E **79**, 031926 (2009)
Lubensky, T.C., Prost, J.: Orientational order and vesicle shape. J. Phys. II Fr. **2**, 371–382 (1992)
Macdonald, C.B., Ruuth, S.J.: Level set equations on surfaces via the closest point method. J. Sci. Comput. **35**, 219–240 (2008)
Menzel, A.M., Löwen, H.: Traveling and resting crystals in active systems. Phys. Rev. Lett. **110**, 055702 (2013)
Mohamed, M.S., Hirani, A.N., Samtaney, R.: Discrete exterior calculus discretization of incompressible Navier–Stokes equations over surface simplicial meshes. J. Comput. Phys. **312**, 175–191 (2016)
Napoli, G., Vergori, L.: Extrinsic curvature effects on nematic shells. Phys. Rev. Lett. **108**, 207803 (2012)
Napoli, G., Vergori, L.: Surface free energies for nematic shells. Phys. Rev. E **85**, 061701 (2012)
Nelson, D.R.: Order, frustration, and defects in liquids and glasses. Phys. Rev. B **28**, 5515–5535 (1983)
Nelson, D.R.: Towards a tetravalant chemistry of colloids. Nano Lett. **2**, 1125–1129 (2002)
Nguyen, T.S., Geng, J., Selinger, R.L.B., Selinger, J.V.: Nematic order on a deformable vesicle: theory and simulation. Soft Matter **9**, 8314–8326 (2013)

Nitschke, I.: Diskretes Äußeres Kalkül (DEC) auf Oberflächen ohne Rand, Diploma thesis, Technische Universiät Dresden, Dresden, Germany (2014). http://nbn-resolving.de/urn:nbn:de:bsz:14-qucosa-217800
Nitschke, I., Reuther, S., Voigt, A.: Discrete exterior calculus (DEC) for the surface Navier–Stokes equation. arXiv Preprint, arXiv:1611.04392 (2016)
Nitschke, I., Voigt, A., Wensch, J.: A finite element approach to incompressible two-phase flow on manifolds. J. Fluid Mech. **708**, 418–438 (2012)
Olshanskii, M.A., Reusken, A., Xu, X.: On surface meshes induced by level set functions. Comput. Vis. Sci. **15**, 53–60 (2013)
Oswald, P., Pieranski, P.: Nematic and Cholesteric Liquid Crystals: Concepts and Physical Properties Illustrated by Experiments, Liquid Crystals Book Series. CRC Press, Boca Raton (2005)
Ramaswamy, R., Jülicher, F.: Activity induced travelling waves, vortices and spatiotemporal chaos in a model actomyosin layer. Sci. Rep. **6**, 20838 (2016)
Rätz, A., Röger, M.: Turing instabilities in a mathematical model for signaling networks. J. Math. Biol. **65**, 1215–1244 (2012)
Rätz, A., Voigt, A.: PDE's on surfaces—a diffuse interface approach. Commun. Math. Sci. **4**, 575–590 (2006)
Rätz, A., Voigt, A.: A diffuse-interface approximation for surface diffusion including adatoms. Nonlinearity **20**, 177–192 (2007)
Reuther, S., Voigt, A.: The interplay of curvature and vortices in flow on curved surfaces. Multiscale Model. Simul. **13**, 632–643 (2015)
Ruuth, S.J., Merriman, B.: A simple embedding method for solving partial differential equations on surfaces. J. Comput. Phys. **227**, 2118–2129 (2008)
Schaeffer, N.: Efficient spherical harmonic transforms aimed at pseudospectral numerical simulations. Geochem. Geophys. **14**, 751–758 (2013)
Segatti, A., Snarski, M., Veneroni, M.: Equilibrium configurations of nematic liquid crystals on a torus. Phys. Rev. E **90**, 012501 (2014)
Segatti, A., Snarski, M., Veneroni, M.: Analysis of a variational model for nematic shells. Math. Model. Methods Appl. Sci. **26**, 1865–1918 (2016)
Stenger, F.: Meshconv, a mesh processing and conversion tool (2016). https://gitlab.math.tu-dresden.de/iwr/meshconv. Computer software
Stöcker, C.: Level set methods for higher order evolution laws. Ph.D. thesis, Technische Universität Dresden, Germany (2008)
Stöcker, C., Voigt, A.: Geodesic evolution laws—a level set approach. SIAM Imaging Sci. **1**, 379 (2008)
Stoop, N., Lagrange, R., Terwagne, D., Reis, P.M., Dunkel, J.: Curvature-induced symmetry breaking determines elastic surface patterns. Nat. Mater. **14**, 337 (2015)
Suda, R., Takami, M.: A fast spherical harmonics transform algorithm. Math. Comput. **71**, 703–715 (2002)
Valette, S., Chassery, J.M., Prost, R.: Generic remeshing of 3D triangular meshes with metric-dependent discrete Voronoi diagrams. IEEE Trans. Vis. Comput. Graph. **14**, 369–381 (2008)
Valette, S., Chassery, J.M., Prost, R.: ACVD, Surface Mesh Coarsinging and Resampling (2014). https://github.com/valette/ACVD. Computer software
VanderZee, E., Hirani, A.N., Guoy, D., Ramos, E.A.: Well-centered triangulation. SIAM J. Sci. Comput. **31**, 4497–4523 (2010)
Vey, S., Voigt, A.: AMDiS: adaptive multidimensional simulations. Comput. Vis. Sci. **10**, 57–67 (2007)
Vitelli, V., Nelson, D.R.: Nematic textures in spherical shells. Phys. Rev. E **74**, 021711 (2006)
Witkowski, T., Ling, S., Praetorius, S., Voigt, A.: Software concepts and numerical algorithms for a scalable adaptive parallel finite element method. Adv. Comput. Math. **41**, 1145–1177 (2015)